NEAR FIELD BEHAVIOR OF REACTING FREE JETS

by

Jeffrey Russell Blair

Thesis submitted to the Faculty of the

Virginia Polytechnic Institute and State University

in partial fulfillment of the requirements for the degree of

Master of Science

in

Mechanical Engineering

APPROVED:

Dr. E. F. Brown, Chairman

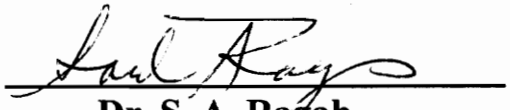

Dr. S. A. Ragab

Dr. U. Vandsburger

c.2

LD
5655
V855
1995
B535
C. 2

NEAR FIELD BEHAVIOR OF REACTING FREE JETS

by

Jeffrey Blair

Committee Chairman: Eugene F. Brown
Department of Mechanical Engineering

(ABSTRACT)

Numerical simulations of a nonreacting circular jet and both nonreacting and reacting elliptical jets have been completed. Linear stability analysis was used to force the jets at their most amplified frequency. Circular jet simulations showed low levels of coherent structure formation and little oxidizer entrainment. The nonreacting elliptical jet exhibited out-of-plane vortex dynamics and subsequently, structure merging primarily contained within the minor axis region. Chemical reaction hindered out-of-plane vortex motion causing the reacting jet to form primarily planar vortex rings. The overall structure and level of vorticity of the jet was reduced as a result of chemical reaction. Hydroxyl radical production was primarily concentrated within the vortex structures, as expected, but iso-surfaces of hydroxyl number density showed a planar ring shape indicating that the structures were, in fact, planar.

Acknowledgments

First, I am thankful to Dr. Brown for his help and guidance throughout the extent of this project. Also, I would like to express my gratitude for the assistantship he provided, and to Dr. S. A. Ragab and Dr. U. Vandsburger for their serving on my advisory committee. I would also like to thank the Office of Naval Research for providing the funds to make this work possible, and for providing the CM-5 supercomputer for the simulations. I am grateful to Dr. B. Ganeshan and Dr. F. F. Grinstein for their guidance with the chemistry.

Next, I would like to acknowledge and thank the supervisors of the computer laboratories at Virginia Tech, as they were an integral part of the project. In particular they were used to analyze the data, write this thesis and act as gateway to the CM-5 parallel supercomputer at the Naval Research Laboratory in Washington, D. C. I thank Dr. Ron Kriz and Mike Butsch for their upkeep of the scientific visualization laboratory and Mary Kafura and Ben Poe for their help and assistance in the MECA lab.

I would like to thank my families for their love and support throughout the duration of my work.

Finally, and most importantly, I would like to thank my wife, Kathi, for her love and support throughout.

Table of Contents

List of Tables and Figures

Section 1. Introduction

Section 2. Governing Equations and Chemistry

Section 3. Computer Hardware and Code

Section 4. Simulation Setup

Section 5. Reacting and Nonreacting Flow Results

Section 1: Introduction

Section 1.1. Introduction to Free Jet Flows

This work addresses the behavior of jets found in combustors similar to those found in gas turbine engines. In such devices, jets of vaporized fuel mix with the surrounding air and react exothermically to produce high temperature combustion products. These combustion products are subsequently expanded through a nozzle producing thrust.

Although there are many other examples of reacting systems, we will only concern ourselves with free gaseous jet flows. It is here, where the fuel and oxidizer are generally separated, that the fluid dynamic and chemical coupling becomes important.

Anderson [1] cites a number of other examples where high temperature reacting flows are important. Rocket engines, as shown in the schematic of Figure 1.1, illustrate a classic example of the role of jet mixing and chemical reaction. Typically one would like high mixing between the fuel and oxidizer and therefore, efficient combustion with little

unreacted fuel and oxidizer leaving the combustion chamber. If the combustion chamber can realize more efficient combustion, a higher temperature product will be formed, resulting in an increase in thrust. Alternatively, an equivalent product temperature in a smaller combustion chamber would result in lighter propulsion systems and therefore, greater range.

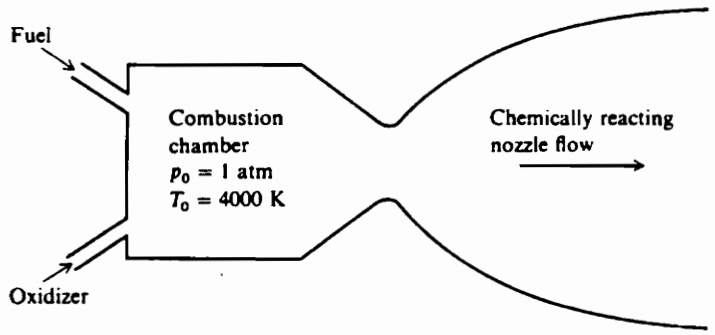

Figure 1.1. Schematic of a rocket engine [1]

An application that one would not normally associate with free jet flows is in high-powered chemical lasers. A stream of atomic fluorine and a stream of molecular hydrogen flow into a mixing region where reaction occurs (See Figure 1.2). Production of excited hydrogen fluoride in the mixing region provides a laser medium. Placing mirrors on either side of the flow in this laser medium produces a high powered laser.

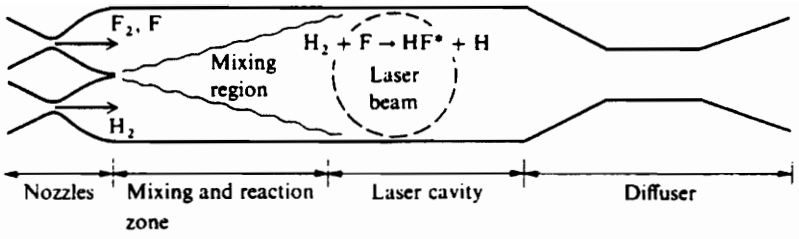

Figure 1.2. Schematic of a Chemical Laser [1]

Supersonic combustion ramjet engines (SCRAMjet), as shown in Figure 1.3, provide an example of a free jet application directly applicable to the present work. If one can increase the mixing between the fuel and oxidizer and therefore, increase combustion efficiency, the SCRAMjet's thrust will be increased.

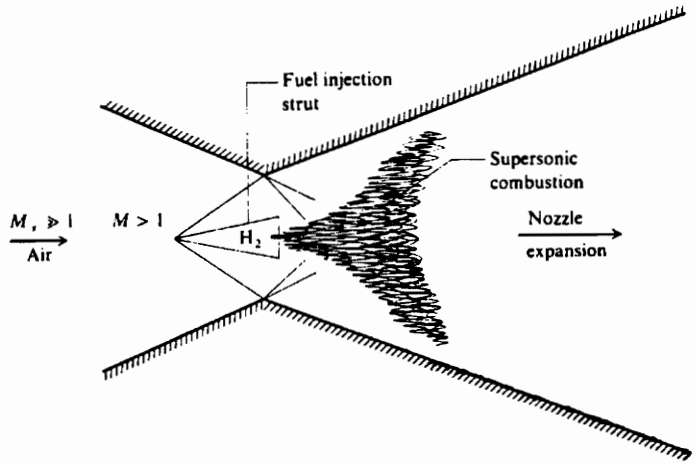

Figure 1.3. Schematic of a supersonic combustion ramjet engine [1]

Jet flows have been an important research focus for many years, and because of the need for smaller, more efficient combustors, fluid dynamic control to increase fuel

and oxidizer mixing is an important topic. Experimental and numerical investigations aimed at optimum control of the combustion zone have been performed for decades. In the present work, just as in many of the previous studies, the confining walls of the combustor are assumed to be infinitely far from the jet. This is the so-called free jet assumption. The present work also utilizes prior knowledge of free jet control and uses this information to investigate new facets of fluid dynamic control of reacting free shear layers. In the next few sections, a more in-depth analysis of shear flow instabilities and prior efforts to control these instabilities will be assessed.

Flow instabilities initiate the breakup of an initially laminar jet. The primary instabilities are a result of an inflection point in the jet's velocity profile, making the flow inherently unstable. Spatially dependent instabilities grow in magnitude causing the initially laminar jet to exhibit an uncontrolled, chaotic behavior characteristic of turbulence. To enhance combustion and increase combustion efficiency, control of mechanisms responsible for instability growth is desirable. A combination of large-scale engulfment of the surrounding oxidizing fluid into the fuel jet by the large-scale coherent vortices and small-scale mixing of the fuel and oxidizer is the key to increasing combustor performance.

Two types of jet control are possible: active control and passive control. Active control requires energy input where passive control does not. Active jet control can

initiate desirable forcing patterns at the nozzle exit and causes significant changes in jet structure downstream of the forcing location. For example, controlled pairing of coherent (large-scale) vortices may be possible using an active control scheme.

Passive jet control involves alteration of jet nozzle geometry or shear layer distribution and requires no energy input. Mutter [2] studied this type of jet control and determined ways of increasing jet entrainment. Huang [3] used linear stability analysis to examine the effects of passive jet control. The contributions of both Mutter and Huang will be assessed in later sections.

Section 1.2. Causes of Free Jet Transition

The breakdown of an initially laminar jet to turbulence is known as transition. This transition of a jet to turbulence is a result of the growth of spatially dependent instabilities that grow in magnitude as the flow proceeds downstream. The primary instability is wavelike in nature, and leads to roll-ups in the jet's shear layer. Figure 1.4 shows the roll-up of the shear layer in the near field of the jet. Secondary instabilities that induce the growth of streamwise vorticity develop as the jet moves downstream and ultimately increase the entrainment capabilities of the jet. It is after the secondary

instabilities become significant that the jet takes on a less structured nature and small scale structures begin to dominate.

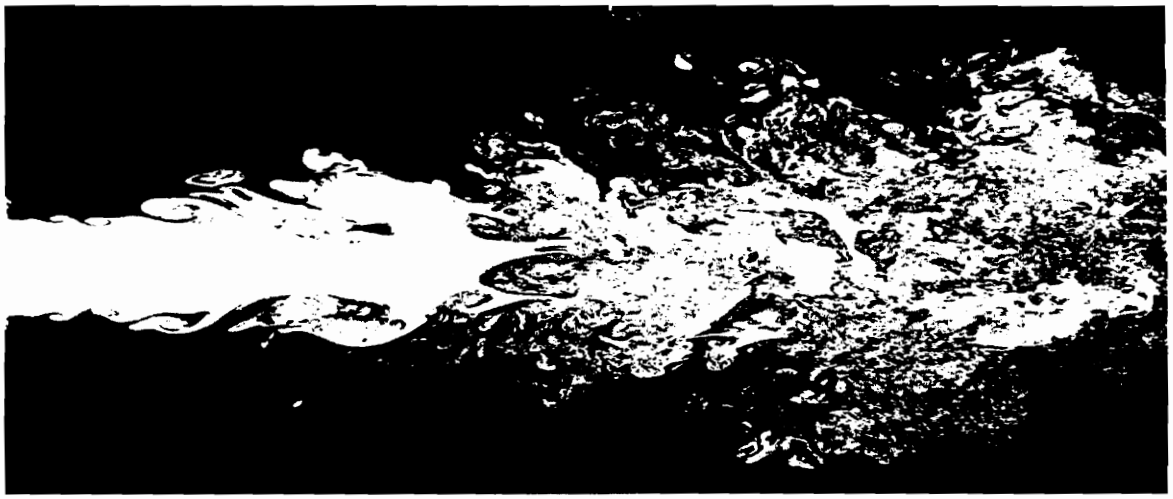

Figure 1.4. Free Air Jet [4]

Bayly et al. [5] studied the instability mechanisms in shear flows. In Bayly's free shear flow research, the primary periodic instability imposed on the basic velocity caused roll-up of the Kelvin-Helmholtz instability waves, and ultimately, these waves rolled up into large-scale vortical structures. These large scale vortical structures persisted into the turbulent region of the far field where they were termed coherent structures. Ho & Huerre [6] studied the dynamics of a perturbed planar free shear layer. Planar shear layers show many of the features seen in free jet flows and therefore, contain many of the physical features that will be encountered in the present work. They found that the production of large scale structures was terminated at the streamwise position where the magnitude of the instabilities at the fundamental frequency becomes maximum. At this saturation point of the fundamental harmonic, the generation of a subharmonic

disturbance was initiated. Ho & Huerre stated that *the excitation of a large subharmonic disturbance can be accounted for by appealing to a secondary subharmonic resonance mechanism that arises when the fundamental f_n has reached its equilibrium level.* The growth of the subharmonic instability led to pairing of large-scale structures at a downstream location where the subharmonic instability reached a peak [7]. Hussain & Husain [8] used flow visualization to study the pairing mechanism in elliptical jets. They showed that on the major plane vortex merging occurred in a predicted manner, the trailing vortex caught the leading vortex and the two merged to form a single larger vortex. On the minor axis, merging was found not to occur in the same fashion. Here the trailing vortex was seen to race by the leading vortex and then break up violently. Hussain & Husain explained this pairing phenomenon by arguing that the vortices become entangled on the major axis and then merge by diffusional processes. They stated that the process of violent breakdown appears to enhance small-scale mixing in elliptical jets.

Three dimensional instabilities produced in the nonlinear region of the jet also have a profound effect on the transition to turbulence in free jets. According to Lin & Corcos [9] streamwise vortices are produced in the braid region between large scale structures. Local strains induced by the presence of the large scale structures are determined to produce the streamwise vortices. They attributed the formation of these streamwise structures to the onset of mixing transition. Monkewitz and Pfizenmaier [10] and Liepmann [11] also suggested that the development of streamwise vorticity initiated the breakdown of laminar jets. The development of streamwise vortex pairs in the braid region of the jet induced the formation of sides jets whose strength is proportional to the circulation of the primary vortex rings.

Ho & Huerre [6] suggested that the transition to small-scale flow originates in the cores of the large-scale structures. Hussain and Husain [8] offered a similar assessment. Their findings showed that the peaks of phase-average incoherent turbulence intensities occurred near the center of the large-scale structure. This production of turbulence was attributed to the interaction of the streamwise ribs located between coherent structures and the coherent structures themselves. They stated that *turbulence produced by the stretching of ribs is advected towards the center of the rolls, resulting in peak values of incoherent turbulence intensities near the roll center.* Reynolds stresses were also determined to be produced by stretching of ribs between coherent vortices. In elliptical jets, stretching of the ribs was found to be greater on the major axis than on the minor and therefore have a higher intensity of Reynolds stress production. Melander and Hussain [12] suggested a coupling between large-scale coherent structures and the surrounding small-scale field. Large-scale structures induced a local strain in the flow, thus organizing the smaller scale structures. The smaller structures formed braids around the coherent vortex in a highly polarized (either left-handed or right handed) fashion.

Huang & Ho [13] studied pairing of spanwise and streamwise vortices and found that this pairing leads to increased levels of small scale eddies. Although much needs to be learned about fluid flow transition to turbulence and turbulence itself, the summary detailed above demonstrates a sense of how researchers assess transition to turbulence.

Section 1.3. Prior Research in Reacting and Nonreacting Free Jets

Prior research on free jet flows can be split into two distinct areas: nonreacting and reacting flows. Nonreacting flows, or cold flows, typically address fluid dynamic effects on the flow field and hypothesize the effects of fluid dynamics on chemistry. Reacting flows couple fluid dynamics and chemistry and more accurately assess the effects of combustion on the flow. First, nonreacting flow research will be considered.

Section 1.3.1 Nonreacting Free Jets and Mixing Layers

Vuillermoz and Oran [14] completed direct numerical simulations of a supersonic mixing layer focused on the effects of viscosity and diffusion on the relevant scales in the flow. Their results revealed three distinct regions in the flow, an initially unstable laminar regime, a convective-mixing regime, and a diffusive mixing regime. Resolution tests suggested that accurate resolution was realized in each of the three regimes for a grid size of 10×10^{-5} m. Additional tests between a full Navier-Stokes simulation and Euler equation governed flow were performed to investigate the effects of molecular diffusion and thermal conduction. The simulations used a Flux Corrected Transport Algorithm to evaluate the convective transport. They stated that *the nonlinear filter in the FCT algorithm acts like a subgrid model that correctly handles the decay of the small scales and their dissipation to heat, thereby mimicking the Kolmogorov scale but at a larger wavelength. When Navier-Stokes and Euler computations agree in the diffusive-mixing regime, it is a sign that the residual numerical dissipation in the algorithm is somewhat*

equivalent to the physical dissipation. Diffusional effects proved to be significant in the laminar regime and in the diffusive mixing regime and relatively less important in the convective-mixing regime. Small scale molecular diffusion dominated the flow in the jet far field and therefore, was logical that binary diffusion should play an important role. Grinstein and Guirguis [15] submitted similar findings. They investigated the effects of the residual numerical viscosity inherent in the explicit FCT algorithm. Concurring with Vuillermoz and Oran, Grinstein and Guirguis sustained the hypothesis that the residual numerical diffusion accurately models physical viscosity. They found that the numerical diffusion most accurately imitated physical viscosity at relatively high Reynolds numbers.

Grinstein et. al. [16] produced a two dimensional numerical study of the transition region of a subsonic, axisymmetric free jet. The effects of initial conditions, excitation, and Mach number on the coherent structures were considered. Self-excitation of the jet caused merging of large-scale structures and instantaneous pressure drops were found to be significantly higher in this merging region than in the rest of the jet. The increased pressure drops in these regions produced streamwise momentum flux increases in the jet transition region.

Of particular interest, in the realm of reacting flows, is the entrainment and mixing properties of free jets. Numerous numerical and experimental efforts aimed at enhancing or understanding entrainment and its properties have been performed previously. Large-scale coherent vortices provide a mechanism for engulfment of ambient fluid into the jet. Additional entrainment results from production of streamwise vortices.

Grinstein, Oran and Boris [17] presented numerical simulation results of a planar shear layer created by coflowing streams past a splitter plate. They concentrated their efforts on coherent structure development and evolution. The simulations showed that the coherent vortices entrained more fast fluid than slow fluid and that the difference in entrainment of fast fluid and slow fluid advanced as the velocity difference increased.

Although all free jets exhibit roll-up of the Kelvin-Helmholtz instability into large-scale azimuthal or spanwise vortices, not all free jets develop significant streamwise vorticity. As mentioned previously, streamwise vorticity production augments turbulence production and therefore transition [9,10,11]. These investigators also suggested that increased streamwise vorticity production increases entrainment. Grinstein et. at. [18] evaluated the effects of spanwise excitation on streamwise vorticity production and therefore, entrainment rates.

Mutter [2] performed fully three-dimensional non-reacting free jet simulations. He compared entrainment rates of circular jets and elliptical jets with uniform and non-uniform momentum thickness distributions at the nozzle exit. Linear stability analysis [3] solutions forced the jets (circular and both elliptical jets) at its most amplified frequency and provided the simulations with a realistic inlet boundary condition (here inlet refers to the inlet of the computational region). In Mutter's simulations, the results of linear stability theory were used to both initialize the flow field and to provide the source of excitation. Mutter found that the non-uniform momentum thickness elliptical jet entrained the most fluid of the three cases studied. He attributed the increased entrainment capabilities of the non-uniform momentum thickness elliptical jet to its

increased production of streamwise vorticity. He found that azimuthal non-uniformities inherent in elliptical jets enhance streamwise vorticity production and therefore increase entrainment. The entrainment rates of the non-uniform momentum thickness elliptical jet tabulated by Mutter closely resembled experimental results of Ho & Gutmark [19].

Section 1.3.2 Reacting Free Jets and Mixing Layers

Because of the need for efficient combustors, many numerical and experimental efforts have been made at understanding the characteristics of entrainment and mixing in reacting free jets. Within the scope of reacting flows, heat release and fluid dynamic effects, such as vortex dynamics, have been the primary focus of reacting flow analyses. The following paragraphs assess the efforts of previous research as they relate to the present work.

McMurtry et. al. [20] studied the effects of heat release on a two-dimensional mixing layer. The simulations employed periodicity in the streamwise direction with free-slip boundary conditions in the transverse plane. The chemistry included a single-step irreversible chemical reaction of two reactants producing a single product with heat release and a reaction rate dependent on reactant concentrations only. Chemical energy release proved, as has been found by many other investigators, to cause significant decreases in the growth rate of the mixing layer as well as significant decreases in product production. The vorticity field also showed notable changes as a result of exothermicity, and in particular, heat release decreased the vorticity at the center of the large-scale coherent structures and caused the vorticity field to become less structured.

Sekar and Mukunda [21] found that heat release does not severely retard mixing in high speed flows. Direct numerical simulations of reacting H_2 and air with convective Mach numbers of 0.38 and 0.76 showed that heat release affected flow dynamics less as the convective Mach number was increased. Heat release reduced the convective speed of the flow from 3 - 10 %, reduced the growth rate by only 7 %, and diminished the entrainment by 25 %. Although many of the effects of heat release presented in other works are qualitative, the findings of Sekar and Mukunda seem to lessen the importance of heat release on flow dynamics.

Grinstein and Kailasanath [22,23] demonstrated the effects of chemical exothermicity on shear layer growth, product formation and temperature change. A two-dimensional numerical simulation was performed on a reactive shear layer using hydrogen and oxygen as the fuel and oxidizer, respectively. In agreement with other work on reacting shear flows, chemical energy release proved to hinder shear layer growth and product formation. Convective effects due to the differences in stream speeds caused product formation to shift toward the slower stream. Soteriou and Ghoniem [24] made a similar assessment. Results showed the chemical heat release reduced the effective mixing capabilities and diminished turbulence levels in the jet. Heat release also caused increased streamwise flow acceleration as a result of density gradients.

Vuillermoz et al. [25] investigated the effects of Damköhler number on a supersonic reactive mixing layer. The Damköhler number is the ratio of the relative reaction time to the species mixing time. They described two mixing regimes: a convective mixing regime and a diffusive mixing regime. For large Damköhler number, fast chemistry, the flame was contained to the convective mixing regime and dominated

by large scale mixing. Alternatively, for small Damköhler number, the flame continued to burn into the diffusive mixing regime where smaller scales dominate the flow field.

Section 1.3.3 Density Ratio Effects on Shear Layer Development

Russ and Strykowski [26] investigated the effects of initial conditions on jet development and mixing. Experimental tests showed that a decrease in the initial jet to ambient density ratio from 1.0 to 0.5 resulted in a faster breakup of the jet with significantly increased shear layer growth. The increased spreading and quicker breakup of the jet was attributed to the formation of side-jets on the coherent vortex rings. Monkewitz et al. [10] determined the inception of side-jets to be a result of growth of the Widnall instability found in vortex structures. Additionally, Monkewitz and Sohn [27] evaluated the stability properties of hot jets with non-unity density ratios. Jets with a density ratio of less than 0.72 times the surrounding free stream or ambient density were found to be absolutely unstable. This resulted in self-excitation of the jet, or, in other words, instability growth as a result of jet dynamics and not forced excitation. Adding to the work of Monkewitz and Sohn, Kyle and Sreenivasan [28] discovered an oscillatory instability in the shear layer region of jets with a density ratio of less than 0.6.

Section 2: Governing Equations and Chemistry

Section 2.1. Governing Equations

Analysis of the entrainment process in free jet flows encompassed the focus of the prior work on this particular free jet research. Since entrainment is primarily an inviscid mechanism, the inviscid equations of fluid motion, the Euler equations, were used previously and will be used in the present simulations. The residual numerical diffusion inherent in the FCT algorithm effectively models physical viscosity [14,15], and therefore, for all intents and purposes, minor viscous effects are present. Oran and Boris [29,30] provide a more in-depth account of the equations describing reacting fluid flows and suggest many of the references cited in section 2.

The equations governing the mass density (ρ), the individual chemical number species (n_i), the momentum density ($\rho\vec{v}$), and the energy density (E) are given below.

$$\frac{\partial \rho}{\partial t} = -\nabla \cdot (\rho \vec{v}) \qquad (2.1)$$

$$\frac{\partial n_i}{\partial t} = -\nabla \cdot (n_i \vec{v}) - \nabla \cdot (n_i \vec{v}_{di}) + Q_i - L_i n_i \qquad i = 1,...,N_s \qquad (2.2)$$

$$\frac{\partial \rho \vec{v}}{\partial t} = -\nabla \cdot (\rho \vec{v} \vec{v}) - \nabla \cdot \overline{\overline{P}} \qquad (2.3)$$

$$\frac{\partial E}{\partial t} = -\nabla \cdot (E \vec{v}) - \nabla \cdot \left(\vec{v} \cdot \overline{\overline{P}}\right) - \nabla \cdot \vec{q} \qquad (2.4)$$

In the above equations, ρ is the mass density, $\vec{v}$ is the local fluid velocity, n_i is the individual species number density, $\vec{v}_{di}$ is the species diffusion velocity, Q_i is the rate of production of species i as a result of chemical reaction, L_i is the chemical loss rate of species i, $\overline{\overline{P}}$ is the pressure tensor, E is the energy density, and $\vec{q}$ is the heat flux vector. In each of the equations, the "over arrow" denotes a vector, while the double overbar depicts a tensor quantity.

The pressure tensor is given by

$$\overline{\overline{P}} \equiv P\overline{\overline{I}} \qquad (2.5)$$

where P is the thermodynamic pressure. The heat flux vector is defined as the following.

$$\bar{q}(N,T) \equiv -\lambda_m \nabla T + \sum_i n_i h_i \bar{v}_{di} \qquad (2.6)$$

A sum of the kinetic energy and internal energy generates the total energy density, E, where the total internal energy, $\rho\varepsilon$, results from the difference between the total internal enthalpy and the thermodynamic pressure.

$$E \equiv \frac{1}{2}\rho\bar{v}\cdot\bar{v} + \rho\varepsilon \qquad (2.7)$$

$$\rho\varepsilon = \sum_i \rho_i h_i - P \qquad (2.8)$$

The rate of production and chemical loss rate of species n_i are given by,

$$Q_i = \sum_j k_{i,j} n_j + \sum_{j,k} k_{i,jk} n_j n_k + \sum_{j,k,l} k_{i,jkl} n_j n_k n_l \qquad (2.9)$$

$$L_i = k_i^r + \sum_j k_{i,j}^r n_j + \sum_{j,k} k_{i,jk}^r n_j n_k \qquad (2.10)$$

where k is the chemical reaction rate constant. For this analysis, the terms Q_i and $L_i n_i$ have been grouped into a net production rate, ω_i..

$$\omega_i = Q_i - L_i n_i \qquad (2.11)$$

To relate pressure, temperature, and mass density or species number density we assume the ideal gas equation of state.

$$P = N k_B T = \rho \overline{R} T \qquad (2.12)$$

N is the total number of molecules in the mixture, k_B is the Boltzman's constant, T is temperature, and $\overline{R}$ is the universal gas constant. The caloric equation of state supplies the needed relation between specific enthalpy and temperature.

$$h_i = h_{i_o} + \int_{T^o}^{T} c_{p_i} dT \qquad (2.13)$$

In the above equation, h_i is the i^{th} specie-specific enthalpy, h_{io} is the heat of formation of species i evaluated at the reference temperature, T^o. c_{pi} is the constant pressure specific heat of species i.

The fluid is assumed to be a continuum, i.e., the equations cannot describe physics on the order of the mean free path of the molecules. Viscous effects are neglected. All external forces, such as gravitational effects, are neglected. Thermal diffusion effects are assumed small and are neglected. Radiative heat flux is assumed negligible.

Section 2.2. Specific Heats, Heats of Formation, and Enthalpy

A second order polynomial fit of the specific heat data supplied by Chase et al. [31] from 1000 K to 4000 K yielded the needed temperature dependent specific heat relation. Likewise, a second order polynomial fit of each specie's internal enthalpy [32] produced the internal enthalpy as a function of temperature for the evaluation of heat release terms. The following tables show the data, heats of formation, and the second order approximations of Δh. Following the tables are plots of the specific heats and Δh for each species as well as the error in using the 2^{nd} order polynomial approximations. Notice from the plots, that the polynomial approximations reproduce actual specific heat and enthalpy values quite accurately within the temperature range of most regions of the jet (1400 K - 2800 K). Most errors are well below 1 % in this range.

Table 2.1. 2^{nd} order approximation to cpi

Species	*2^{nd} Order Approximation to $c_{pi}(T)$*
	(J/K/mol)
H_2	$-5.4938\times10^{-7}\ T^2 + 5.6879\times10^{-3}\ T + 25.027$
O_2	$-2.9157\times10^{-7}\ T^2 + 3.5785\times10^{-3}\ T + 31.759$
OH	$-7.2503\times10^{-7}\ T^2 + 5.9169\times10^{-3}\ T + 25.619$
H_2O	$-1.8952\times10^{-6}\ T^2 + 1.4676\times10^{-2}\ T + 29.093$
N_2	$-6.4173\times10^{-7}\ T^2 + 4.5830\times10^{-3}\ T + 29.219$

Table 2.2. 2^{nd} order approximation to Δh

Species	*Heat of Formation (@ 298 K)*	*Δh(0 K - 298 K)*	*2^{nd} Order Approximation to $\Delta h(T)$ (298 K - temp)*
	(kJ/kmol)	(J/K/mol)	(J/K/mol)
H_2	0	8467.	$1.4793\times10^{-3}\ T^2 + 28.145\ T - 9170.3$
O_2	0	8683.	$1.0609\times10^{-3}\ T^2 + 33.434\ T - 11898.$
OH	38987	9172.	$1.1435\times10^{-3}\ T^2 + 29.806\ T - 10311.$
H_2O	-241826	9904.	$2.5760\times10^{-3}\ T^2 + 40.126\ T - 17488.$
N_2	0	8670.	$6.5649\times10^{-4}\ T^2 + 33.070\ T - 12550.$

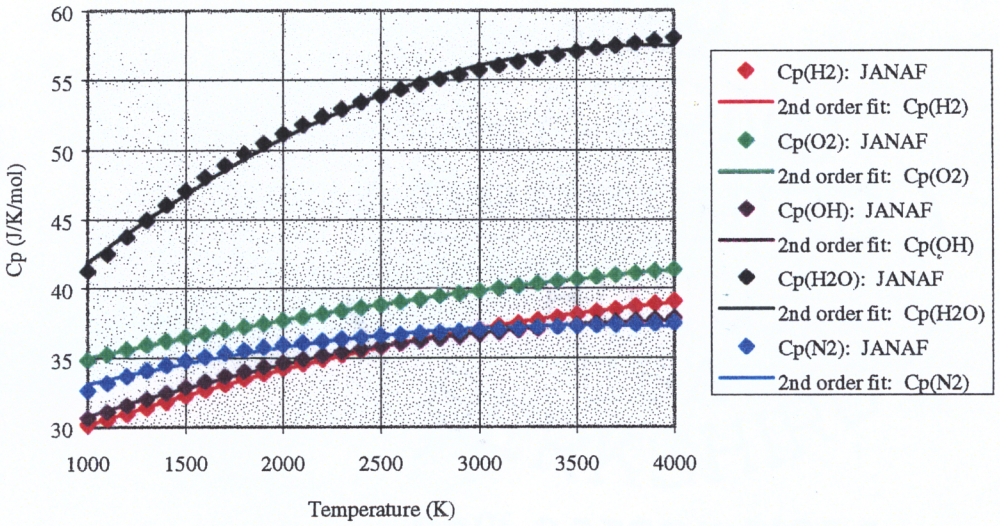

Figure 2.1. Constant pressure specific heat data and polynomial fits of H_2, O_2, OH, H_2O, and N_2 [Data from 31]

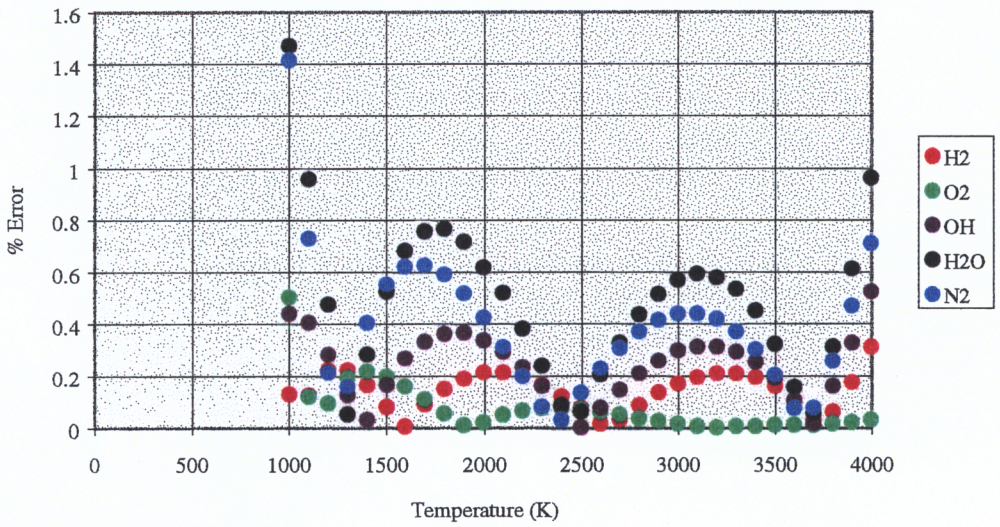

Figure 2.2. Relative errors in the polynomial fit data of c_{pi}

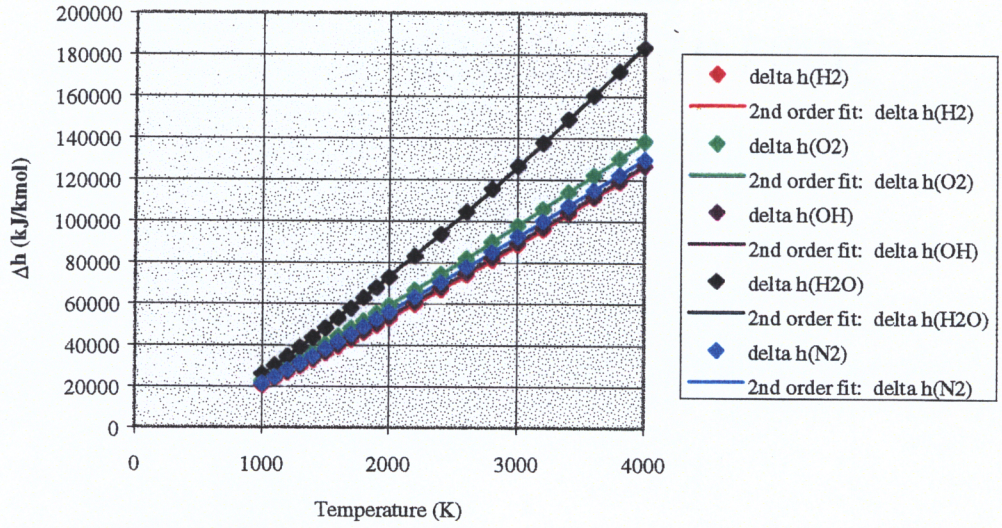

Figure 2.3. Δh (298 K - temp) and 2nd order fits for H_2, O_2, OH, H_2O, and N_2 [Data from 32]

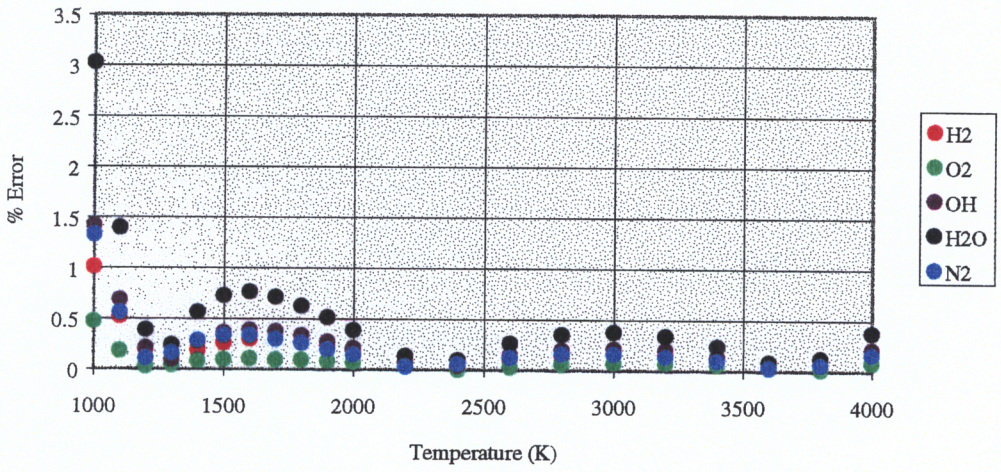

Figure 2.4. Relative errors in the 2nd order fits of Δh

Section 2.3. Species Diffusion

To account for molecular diffusion of the reacting species, the individual species diffusion within the mixture must be determined. The species diffusion velocities are found by inverting the following matrix equation (equation 2.14) subject to the constraint of no net mass flux from interspecies diffusion (equation. 2.15).

$$\vec{G}_i = \sum_k \frac{n_i n_k}{N^2 D_{ik}} \left(\vec{v}_{dk} - \vec{v}_{di} \right) \qquad (2.14)$$

$$\sum_i \rho_i v_{di} = 0 \qquad (2.15)$$

$\vec{G}_i$ is given by,

$$\vec{G}_i \equiv \nabla\left(\frac{n_i}{N}\right) - \left(\frac{\rho_i}{\rho} - \frac{n_i}{N}\right)\frac{\nabla P}{P} \qquad (2.16)$$

To remove the computational strain of calculating the species diffusion velocities as described above, an approximation suggested by Bird, Stewart, and Lightfoot [33] was implemented instead.

$$v_{di} = -\frac{1}{X_i} D_i^m \nabla X_i \qquad (2.17)$$

$$D_i^m = \frac{1 - X_i}{\sum_{j \neq i} X_j / D_{ij}} \qquad (2.18)$$

The above equations describe a generalization to binary Fickian diffusion, in that, the effective binary diffusivity, D_{im}, represents the diffusivity of species i into the mixture. This formulation uses a weighted average of the binary diffusion of species i into species k, where the total average yields the effective binary diffusivity. It should be noted that a zero total momentum flux should have been placed on the molecular diffusion [29], although this should not result in significant errors.

Mason and Marrero [34] give the following expression for the binary diffusion coefficient, D_{ik}, as a function of temperature.

$$D_{ik} = \frac{A_{ik} T^{B_{ik}}}{N} \qquad (2.19)$$

A_{ik} and B_{ik} are species dependant constants used to empirically fit the binary diffusivity coefficient to experimental data.

Section 2.4. Thermal Conduction: λ_m

Fourier's law is incorporated into the energy equation to model heat flux in the flow due to spatial temperature gradients. Since the flow is not homogeneous and temperature gradients exist, a local thermal conduction coefficient dependent on species mixture concentrations and local temperature is needed. Mason and Saxena [35] suggest

$$\lambda_m = \sum_i \lambda_i \left[1 + \frac{1.065}{2\sqrt{2} n_i} \sum_{k \neq i} n_k \phi_{ik} \right]^{-1} \qquad (2.20)$$

where,

$$\phi_{ik} = \frac{\left[1 + \left(\lambda_i^0 / \lambda_k^0\right)^{1/2} \left(m_i / m_k\right)^{1/4}\right]^2}{\left[1 + m_i / m_k\right]^{1/2}} \qquad (2.21)$$

The thermal conductivity of species i may be evaluated from a correlation from Hirschfelder et al.[36].

$$\lambda_i = E_i \lambda_i^0 \qquad (2.22)$$

$$E_i = 0.115 + 0.354 \frac{c_{pi}}{k_B} \qquad (2.23)$$

λ_i^o represents the thermal conductivity of species i with its internal degrees of freedom frozen, i.e. the molecule's thermal conductivity is normalized to its rigid sphere value. The Euken factor, E_i, corrects the frozen thermal conductivity of polyatomic molecules, λ_i^o, by considering the added vibratory and rotational internal energy of polyatomic molecules. c_{pi} is the constant pressure specific heat of species i and k_B is Boltzman's constant. λ_i^0 is found by

$$\lambda_i^0 = \frac{8.322 \cdot 10^3}{\sigma_i^2 \Omega_{ii}^{(2,2)*}} \left(\frac{T}{m_i}\right)^{1/2} \qquad (2.24)$$

σ_i is the collision diameter of species i and m_i is the molecular weight of species i. $\Omega_{ii}^{(2,2)*}$ is a collision integral based on the Lennard-Jones 6-12 potential, φ, that incorporates local deflections of colliding molecules and attractive and repulsive forces between the colliding molecules .

$$\varphi = 4\varepsilon\left[\left(\frac{\sigma}{r}\right)^{12} - \left(\frac{\sigma}{r}\right)^{6}\right] \tag{2.25}$$

Equation 2.25 shows the Lennard-Jones potential. r symbolizes the distance of separation between two molecules, σ represents the molecular diameter normalized to a spherical value, and ε denotes the depth of the potential well or its minimum potential energy. Notice that where molecules are close $(\sigma/r)^{12} >> (\sigma/r)^{6}$ and the molecules repel one another. Conversely, when the molecules are farther apart the $(\sigma/r)^{6}$ term dominates and the molecules attract one another. Figure 2.5 gives a pictorial representation of this explanation.

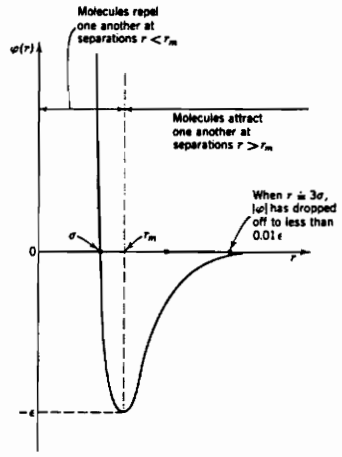

Figure 2.5. Lennard-Jones potential energy function [33]

The Lennard-Jones 6-12 potential energy function is directly applicable to nonpolar gases with minimal error. Polar molecules are more closely represented by a Stockmayer-type potential that accounts for the angular dependence of the potential energy between two polar molecules. The current simulations use the Lennard-Jones 6-12 potential function for all species, including the polar H_2O molecule, because data is readily available for the Lennard-Jones potential. Dixon-Lewis [37] give an approximation of ε_{H_2O} and σ_{H_2O} to the Lennard-Jones potential, thereby, reducing the error in the Lennard-Jones representation of the H_2O molecule's potential energy function.

The $\Omega_{ii}^{(2,2)^*}$ collision integral is a function of the reduced temperature,

$$T_i^* = \frac{k_B T}{\varepsilon_i} \qquad (2.26)$$

ε_i , as described previously, is a constant depending on the interaction of two type i molecules, i.e. the potential well of molecule i. Hirschfelder, Curtiss, and Bird [36] generated a table of the $\Omega_{ii}^{(2,2)*}$ collision integral as a function of the reduced temperature. The plot below shows the $\Omega_{ii}^{(2,2)*}$ collision integral as function of reduced temperature. The 4th order approximation to $\Omega_{ii}^{(2,2)*}$ is given by: $\Omega_{ii}^{(2,2)*} = 2.4747x10^{-7}\ T^{*4} - 3.6692x10^{-5}\ T^{*3} + 1.9319x10^{-3}\ T^{*2} - 4.5258x10^{-2}\ T^{*} + 1.1147.$

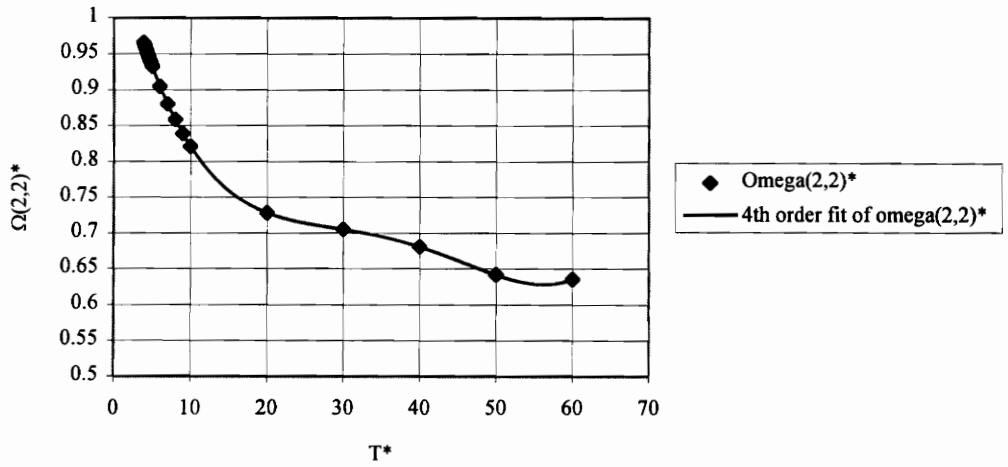

Figure 2.6. $\Omega_{ii}^{(2,2)*}$ ***collision integral as a function of reduced temperature, T*.***

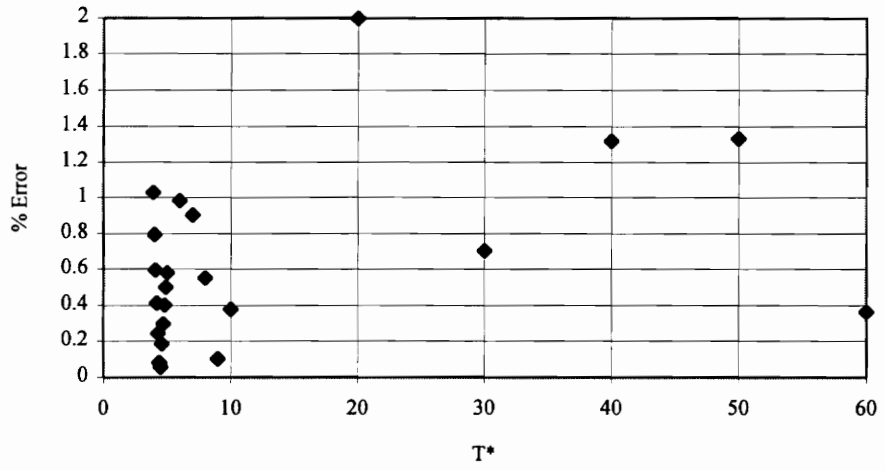

Figure 2.7. Error in the 2nd order polynomial fit of the $\Omega_{ii}^{(2,2)*}$ collision integral as a function of reduced temperature, T*

Section 2.5. Chemical Kinetics

Most reacting systems, such as in the H_2-O_2 system, consist of many intermediate steps before producing the final product. A reaction sequence of this nature is called a chain reaction. An initial reaction, termed the chain initiating reaction, commences the chain reaction, and either chain branching or chain propagating reactions follow the chain initiating reaction. Chain propagating reactions are characterized by an equal number of radicals on either side of the chemical reaction. Chain branching reactions produce a greater number of free radicals than are consumed. Finally, the reaction is terminated via a chain terminating reaction that consume the remaining free radicals from the chain

branching or chain propagating reactions. Kuo [38] provides an excellent review of chemical reactions and their effects.

A typical hydrogen-oxygen reaction may involve scores of reactions. Present computer resources do not allow a fully three dimensional reactive flow simulation of full hydrogen-oxygen chemistry to be completed because storage of each of the constituent species and run time would be exceeding large. For this reason, reduced chemistry models of the full chemistry are used. The present computer simulations have used a two-step reaction suggested by Rogers and Chinitz [39] where a fuel, H_2, and an oxidizer, O_2, react to form a radical, OH. Subsequently, the hydrogen reacts with hydroxyl, OH, to produce the final product, H_2O.

$$H_2 + O_2 \leftrightarrow 2OH \tag{2.27}$$

$$H_2 + 2OH \leftrightarrow 2H_2O \tag{2.28}$$

Vuillermoz et. al. [25] also used this reaction set in modeling a supersonic reacting shear layer. Their reaction rate data was adopted by this work. Table 2.3 shows the reaction rates and equilibrium constants for each reaction. The reverse reaction rates may be obtained from the forward rate and the equilibrium constant.

$$k_1^b = k_1^f / K_1 \qquad (2.29)$$

$$k_2^b = k_2^f / K_2 \qquad (2.30)$$

Table 2.3. Reaction rate and equilibrium constant data for the governing chemical model

	Forward Rate Constant	*Equilibrium Constant*
Reaction 1	$k_1^f = 33.91 \times 10^{41}\ T^{-10}\ e^{-2448/T}$ $(m^3/mol/s)$	$K_1 = 33.78\ e^{-9231.7/T}$
Reaction 2	$k_2^f = 4.25 \times 10^{64}\ T^{-13}\ e^{-21388/T}$ $(m^6/mol^2/s)$	$K_2 = 1.30 \times 10^{-8}\ e^{67615/T}$

Vuillermoz et. al. recognized that the timescale of the first reaction was very small in comparison to a typical convective time scale. This allowed them to assume the first reaction to be in a quasi-equilibrium state during each time step. This approach is followed here. Assumption of equilibrium reduces a first order ordinary differential equation to an algebraic equation. The solution of this algebraic equation follows.

Table 2.4. Changes in equilibrium species number densities for $H_2 + O_2 \leftrightarrow 2OH$

Initial concentration before reaction	n_{H_2}	n_{O_2}	n_{OH}
Change in concentration as a result of reaction assuming instantaneous equilibrium	$-z$	$-z$	$+2z$
Equilibrium concentrations	$n_{H_2} - z$	$n_{O_2} - z$	$n_{OH} + 2z$

Now that the equilibrium number densities can be computed (symbolically), an expression for the equilibrium constant K can be determined.

The equilibrium constant, K_1, as a function of species number density for reaction 1 is given by equation 2.31.

$$K_1 = \frac{(n_{OH} + 2z)^2}{(n_{H_2} - z)(n_{O_2} - z)} \qquad (2.31)$$

Now the above reaction may be solved for the change in species number density of hydrogen and oxygen. The change in hydroxyl number density is just twice the negative of the change in hydrogen or oxygen.

$$z = \frac{K_1\left(n_{O_2} + n_{H_2}\right) + 4n_{OH}}{2\left(K_1 - 4\right)} \pm \frac{\sqrt{\left[K_1\left(n_{O_2} + n_{H_2}\right) + 4n_{OH}\right]^2 - 4\left(K_1 - 4\right)\left(n_{H_2} n_{O_2} K_1 - n_{OH}{}^2\right)}}{2\left(K_1 - 4\right)} \quad (2.32)$$

Notice in the above solution for the change in number density of the reacting species in the first reaction that there are two roots present. The negative sign has been chosen based on the fact that no reaction, and hence, no change in z, can occur if both O_2 and OH are not present.

$$z = \frac{K_1\left(n_{O_2} + n_{H_2}\right) + 4n_{OH}}{2\left(K_1 - 4\right)} - \frac{\sqrt{\left[K_1\left(n_{O_2} + n_{H_2}\right) + 4n_{OH}\right]^2 - 4\left(K_1 - 4\right)\left(n_{H_2} n_{O_2} K_1 - n_{OH}{}^2\right)}}{2\left(K_1 - 4\right)} \quad (2.33)$$

The reaction rates for reaction 2 vary significantly as a function of temperature. For instance, the backward rate increases by 8 orders of magnitude between 1400 and 2300 K, but the forward rate remains on the same order of magnitude throughout this temperature range. Because of the slow backward reaction rate at temperatures on the

order of the initial temperature in the system, 1400 K, the second reaction was not assumed to reach equilibrium instantaneously as in the first reaction. The rate law supplies the rates of production of the species present in the second equation. These production rates are presented below.

$$\omega_{H_2} = - k_2^f n_{H_2} n_{OH}^2 + k_2^b n_{H_2O}^2 \qquad (2.34)$$

$$\omega_{OH} = - 2k_2^f n_{H_2} n_{OH}^2 + 2k_2^b n_{H_2O}^2 \qquad (2.35)$$

$$\omega_{H_2O} = 2k_2^f n_{H_2} n_{OH}^2 - 2k_2^b n_{H_2O}^2 \qquad (2.36)$$

The second reaction integrated explicitly provides the changes in species number density of each of the constituents and when added to the change in species number densities of reaction 1, the total change in each species number density is found. Chemical time step choice is fully detailed in section 3.

Section 3: Computer Hardware and Code

Section 3.1. CM-5 Architecture and Control

The CM-5 is a highly parallel super-computer manufactured by Thinking Machines Corporation for performing parallel computing on large data sets. The CM-5 consists of an array of processing nodes (PN), a number of control processors (CP), and high-speed data networks.

Each CM-5 consists of hundreds or thousands of processing nodes. In particular, the CM-5 used presently in the Naval Research Laboratory in Washington, DC contains 256 single processing nodes. The heart of each processing node is a RISC microprocessor, a CM-5 Network Interface, and four vector units (See Figure 3.1).

A 64-bit bus provides communication between the processor, the vector units and the network interface. Each PN contains two vector unit chips each of which consists of two vector units with accessibility to a total of 128 Mbytes of memory. Each vector unit acts as a memory manager as well as a vector arithmetic accelerator.

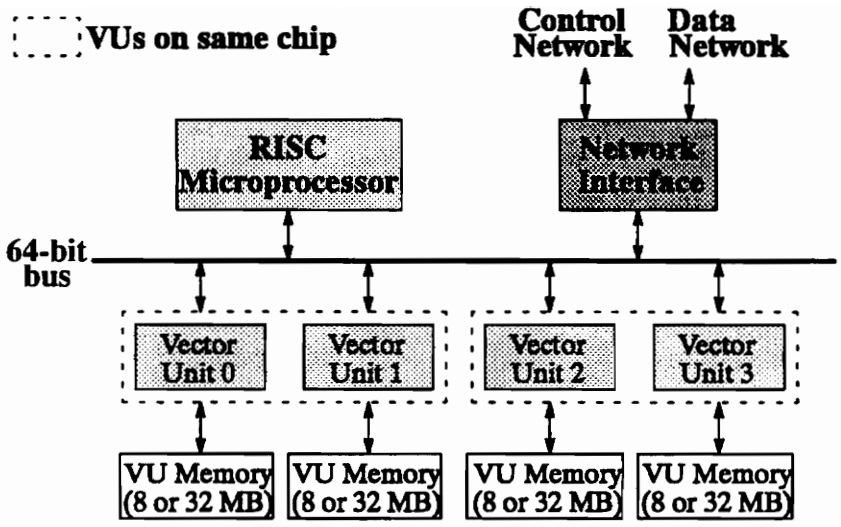

Figure 3.1. Components of a processing node with vector units [40]

To control the partition of processing nodes, each partition is allocated a control processor called a partition manager (PN). The partition manager controls program execution and flow using an enhanced version of the UNIX operating system, CMOST. The partition manager also uses RISC microprocessor technology with local memory used to store scalar data and program code.

The processing nodes and partition managers communicate via two communication networks. The first of these, called the control network, transfers parallel

operations among the processing nodes. The second network, called the data network, transports large data sets from source to destination.

Control processors, called I/O control processors (IOCP), allow communication between the CM-5 and the "outside world" through the data network. External storage devices, such as the Scaleable Disk Array (SDA), and external connections (Ethernet) connections are all managed by the IOCP. The CM-5 supports both HIPPI (HIgh-Performance Parallel Interface) and VME interfaces.

The SDA is an expandable RAID-3 disk storage system consisting of many Disk Storage Nodes. The SDA's Disk Storage Nodes are connected directly to the data network allowing quick and efficient data storage. Disk Storage Nodes may be added to the SDA as needed, and at full capacity, the SDA may provide 200 Gbytes of storage space.

The preceding discussion and the discussion in the following section may be found in greater detail in the CM-5's on-line documentation, CMview [40].

Section 3.2. Parallel Processing

Parallel processing is a fairly new innovation that takes advantage of multiple processors linked through a data network and its ability to process simultaneously, multiple facets of a program. Two types of parallel processing generally are available, control parallelism and data parallelism. Concurrent processing using control parallelism generally instructs different processors to complete different tasks in a program, while data parallelism proves very useful in manipulating large data sets. The data set, generally array valued, is spread across the set of processors allowing each processor to perform the same task on each data subset. The CM-5 supports three parallel programming languages: CM Fortran, C*, and *Lisp, where CM Fortran uses Fortran 90 array definitions. The CM-5 also allows complete portability between CM-5's with different numbers of processors and allows direct portability between the CM-5 and CM-200 , the parallel predecessor of the CM-5.

The CM-5's architecture provides an efficient means for solving sets of equations in a domain discretized into a number of elements. In its SIMD (Single Instruction, Multiple Data) mode, the processing nodes on the CM-5 may be thought of as an array of processing nodes and calculations proceed in the data parallel fashion. The array of data

is laid across processors much in the same way that the data resides in the physical domain. In this array of processors, each instruction is performed concurrently in each processor on each data subset. If the array of data exceeds the number of available processors, each processor divides itself into virtual processors until each element of the array realizes its own virtual processor.

The native mode of the CM-5 is the MIMD (Multiple Instructions, Multiple Data) mode where calculations are conducted in a control parallel fashion.

The previous work on this project employed the SIMD architecture to exploit data parallel advantages on the large 3-dimensional arrays found in the simulations. Also, SIMD architecture allows essentially direct portability between serial and parallel codes whereas the MIMD architecture requires message passing algorithms to control processor instructions. For this work on free jet simulations, the SIMD mode of the CM-5 was used.

Section 3.3. Numerical Integration

Section 3.3.1 1-D Numerical Algorithm for Convection

The governing equations, the Euler equations, are subjected to steep gradients throughout the flow field. In order to preserve these gradients an algorithm capable of maintaining local maximum and minimums with minimal numerical diffusion is required. Most integration methods tend to smear gradients in an unphysical manner across computational cells or produce new maximums or minimums. Oran and Boris [29] provide an in depth analysis of different integration schemes and the results of the steep gradient resolution problem. Mutter [2] presents a helpful synopsis of their findings.

The integration scheme chosen for the present work is the Flux-Corrected Transport (FCT) algorithm developed by Boris and Book [41]. The FCT algorithm is a nonlinear monotone algorithm developed to alleviate the troubles of correctly resolving steep gradients found in many systems governed by a set of continuity equations (See Equations 2.1 - 2.4).

The FCT algorithm insures positivity by applying minimal amounts of numerical diffusion as necessary. Of course, this applied numerical diffusion causes unphysical spreading of the solution. To alleviate this problem, FCT supplies an antidiffusion flux to

remove the applied numerical diffusion. The antidiffusion flux is limited by the local concentrations of the conserved quantities, therefore, preserving positivity and accurately resolving the local quantity gradients.

The algorithm, as derived by Boris and Book, solves one-dimensional continuity equations. Direction/timestep splitting allows generalization of the one-dimensional algorithm to a three-dimensional flow. Direction splitting assumes that the changes in the conserved variables within a single timestep are small and, therefore, the contribution of each direction may be integrated independent of the other directions. Using this technique, the governing Euler equations in the streamwise, x, direction become

$$\frac{\partial \rho}{\partial t} = -\frac{\partial (\rho u)}{\partial x} \qquad (3.1)$$

$$\frac{\partial (\rho u)}{\partial t} + \frac{\partial (\rho u u)}{\partial x} = -\frac{\partial P}{\partial x} \qquad (3.2)$$

$$\frac{\partial (\rho v)}{\partial t} + \frac{\partial (\rho v u)}{\partial x} = 0 \qquad (3.3)$$

$$\frac{\partial (\rho w)}{\partial t} + \frac{\partial (\rho w u)}{\partial x} = 0 \qquad (3.4)$$

$$\frac{\partial n_i}{\partial t} + \frac{\partial (n_i u)}{\partial x} = 0 \qquad (3.5)$$

$$\frac{\partial E}{\partial t} + \frac{\partial (Eu)}{\partial x} = - \frac{\partial (Pu)}{\partial x} \qquad (3.6)$$

The present code uses a predictor-corrector form of the FCT integration scheme. The code convects each of the conserved quantities half of a convective timestep and determines velocities and sources at this timestep midpoint. These predicted values are then used to evaluate the change in quantities throughout the entire timestep.

Timestep splitting allows the contributions of species diffusion, species production as a result of chemical reaction, and thermal conduction to be imposed independent of the FCT integration. Timestep splitting, like direction splitting, assumes the changes in the conserved quantities to be small within a single timestep. The code computes the contributions of these effects after the integration of equations 2.1 - 2.4 and then adds the results to the "new" convected values determined by the FCT algorithm. The integration of the chemical source terms and the diffusive transport terms, such as species diffusion and thermal conduction, will be addressed in later sections.

Section 3.3.2 2-D Numerical Algorithm for Convection

Cross-plane slice plots of total velocity in the work of Mutter [2] showed slightly unphysical velocity contours in the cross-plane far downstream from the nozzle exit. Typically, the velocity contours seemed to be concentrated along each of the cross-plane axes, the *y* and *z* axes. In that work, the integration cycled in following manner: *x, y, z, x, z, y, x, y, z,* etc., where a timestep consisted of an integration in each of the orthogonal coordinates. It was this direction spitting technique that Mutter described as being responsible for this apparently inaccurate representation of the velocity field in the cross-plane far from the nozzle exit.

To alleviate this difficulty, a 2-D FCT algorithm developed by DeVore [42] was implemented. This 2-D algorithm evaluates fluxes at interfaces of a control volume and relevant sources within the control volume to predict the conserved quantity at the next timestep. Figure 3.2 shows a sample control volume as used to integrate the continuity equations.

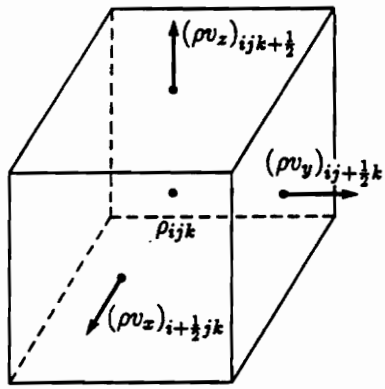

Figure 3.2. Sample control volume used in finite difference approaches to solving continuity equations [42]

The following is a summary of the 2-D FCT algorithm as described by DeVore [42]. First, the solution based on fluxes at the cell interfaces and the previous value is calculated with,

$$\rho_{ij}^{cx} V_{ij}^{\circ} = \rho_{ij}^{\circ} V_{ij}^{\circ} + F_{i-\frac{1}{2}j}^{c} - F_{i+\frac{1}{2}j}^{c} \qquad (3.7)$$

$$\rho_{ij}^{cy} V_{ij}^{\circ} = \rho_{ij}^{\circ} V_{ij}^{\circ} + F_{ij-\frac{1}{2}}^{c} - F_{ij+\frac{1}{2}}^{c} \qquad (3.8)$$

$$\rho_{ij}^{c} V_{ij}^{\circ} = \rho_{ij}^{\circ} V_{ij}^{\circ} + F_{i-\frac{1}{2}j}^{c} - F_{i+\frac{1}{2}j}^{c} + F_{ij-\frac{1}{2}}^{c} - F_{ij+\frac{1}{2}}^{c} \qquad (3.9)$$

where,

$$F^{c}_{i+\frac{1}{2}j} = \rho^{\circ}_{i+\frac{1}{2}j} A^{c}_{xi+\frac{1}{2}j} u_{xi+\frac{1}{2}j} \Delta t \qquad (3.10)$$

In the above equations, V is the cell volume, ρ is the conserved quantity of question, A is the cross-sectional area across which the flux is determined, u is the velocity orthogonal to A, and t is time. The superscript zero denotes the "old" quantities, the superscript c signifies convection, and the $i + 1/2$ locations indicate interface fluid quantities, while i, j and k indicate the three orthogonal directions. Each of the variables not subscripted with an $i + 1/2$ subscript indicate cell centered quantities.

As in the 1-D version of the FCT algorithm, the convected solution is subjected to a diffusive flux dependent on local conserved quantity changes.

$$\rho^{d}_{ij} V^{f}_{ij} = \rho^{c}_{ij} V^{\circ}_{ij} + F^{d}_{i-\frac{1}{2}j} - F^{d}_{i+\frac{1}{2}j} + F^{d}_{ij-\frac{1}{2}} - F^{d}_{ij+\frac{1}{2}} \qquad (3.11)$$

$$F^{d}_{i+\frac{1}{2}j} = \nu_{xxi+\frac{1}{2}j} \left(\rho^{\circ}_{ij} - \rho^{\circ}_{i+1j} \right) V^{f}_{i+\frac{1}{2}j} \qquad (3.12)$$

$$\nu_{xxi+\frac{1}{2}j} = \frac{1}{6} + \frac{1}{3} \varepsilon^{2}_{xi+\frac{1}{2}j} \qquad (3.13)$$

$$\varepsilon_{i+\frac{1}{2}j} = \frac{1}{2} \left(\frac{1}{V^{f}_{ij}} + \frac{1}{V^{f}_{i+\frac{1}{2}j}} \right) u_{xi+\frac{1}{2}j} A^{c}_{xi+\frac{1}{2}j} \Delta t \qquad (3.14)$$

ν, in the above equations, is the coefficient of numerical diffusion, and ε is the local Courant number. Addition of source terms, such as pressure gradients, results in the low-level solution, ρ_{ij}^{l}. Because of the applied diffusive fluxes, the low-level solution suffers from severe spreading. To alleviate this difficulty, an antidiffusional flux is applied to the low-level solution to yield the high-order solution.

$$\rho_{ij}^{h} V_{ij}^{f} = \rho_{ij}^{l} V_{ij}^{f} + F_{i-\frac{1}{2}j}^{a} - F_{i+\frac{1}{2}j}^{a} + F_{ij-\frac{1}{2}}^{a} - F_{ij+\frac{1}{2}}^{a} \qquad (3.15)$$

$$F_{i+\frac{1}{2}j}^{a} = \mu_{xxi+\frac{1}{2}j}\left(\rho_{i+1j}^{cx} - \rho_{ij}^{cx}\right)V_{i+\frac{1}{2}j}^{f} + \mu_{xyi+\frac{1}{2}j}\left(\rho_{i+\frac{1}{2}j+\frac{1}{2}}^{cx} - \rho_{i+\frac{1}{2}j-\frac{1}{2}}^{cx}\right)V_{i+\frac{1}{2}j}^{f} \qquad (3.16)$$

$$\mu_{xxi+\frac{1}{2}j} = \frac{1}{6} - \frac{1}{6}\varepsilon_{xi+\frac{1}{2}j}^{2} \qquad (3.17)$$

$$\mu_{xyi+\frac{1}{2}j} = -\frac{1}{2}\varepsilon_{xi+\frac{1}{2}j}\varepsilon_{yi+\frac{1}{2}j} \qquad (3.18)$$

$$\varepsilon_{yi+\frac{1}{2}j} = \frac{1}{4}\left(\varepsilon_{yij-\frac{1}{2}} + \varepsilon_{yi+1j-\frac{1}{2}} + \varepsilon_{yij+\frac{1}{2}} + \varepsilon_{yi+1j+\frac{1}{2}}\right) \qquad (3.19)$$

$$\rho_{i+\frac{1}{2}j+\frac{1}{2}}^{cx} = \frac{1}{4}\left(\rho_{ij}^{cx} + \rho_{i+1j}^{cx} + \rho_{ij+1}^{cx} + \rho_{i+1j+1}^{cx}\right) \qquad (3.20)$$

μ_{xx} and μ_{xy}, in the above equations, are the antidiffusion coefficients, F^a is the antidiffusive flux, and ε is the interface Courant number, where the Courant number and the convected solution are based on averages of the surrounding cell values (Equations 3.15 - 3.20). Now that the antidiffusive fluxes have been obtained, they must be limited so that new maxima or minima are not produced. First, the maximum and minimum values of the final solution need to be computed.

$$\rho_{ij}^{\max} = \max\left(\rho_{i-1\,j-1}^{l}, \rho_{ij-1}^{l}, \rho_{i+1\,j-1}^{l}, \rho_{i-1\,j}^{l}, \rho_{ij}^{l}, \rho_{i+1\,j}^{l}, \rho_{i-1\,j+1}^{l}, \rho_{ij+1}^{l}, \rho_{i+1\,j+1}^{l}\right) \qquad (3.21)$$

The minimum extrema is computed in a similar fashion. Next, as DeVore explains, *those antidiffusive fluxes that are directed downstream with respect to the local gradient, i.e., which act to smooth the profile rather than steepen it, are canceled. Such fluxes contribute to the formation of dispersive ripples, degrading the quality of the solution. The third step is the calculation of the total antidiffusive fluxes into and out of each cell (P_{ij}) and the maximum allowed fluxes into and out of each cell (Q_{ij}).*

$$P_{ij}^{+} = \max\left(F_{i-\frac{1}{2}j}^{a},0\right) - \min\left(F_{i+\frac{1}{2}j}^{a},0\right) + \max\left(F_{ij-\frac{1}{2}}^{a},0\right) - \min\left(F_{ij+\frac{1}{2}}^{a},0\right) \qquad (3.22)$$

$$P_{ij}^{-} = \max\left(F_{i+\frac{1}{2}j}^{a},0\right) - \min\left(F_{i-\frac{1}{2}j}^{a},0\right) + \max\left(F_{ij+\frac{1}{2}}^{a},0\right) - \min\left(F_{ij-\frac{1}{2}}^{a},0\right) \qquad (3.23)$$

$$Q_{ij}^{+} = \left(\rho_{ij}^{\max} - \rho_{ij}^{l}\right)V_{ij}^{f} \tag{3.24}$$

$$Q_{ij}^{-} = \left(\rho_{ij}^{l} - \rho_{ij}^{\min}\right)V_{ij}^{f} \tag{3.25}$$

Now the ratios of the antidiffusive fluxes are calculated and applied so that new maxima and minima are not produced, and finally, the antidiffusion coefficient, C, is determined.

$$R_{ij}^{+} = \min\left(1, {Q_{ij}^{+}}/{P_{ij}^{+}}\right) \tag{3.26}$$

$$R_{ij}^{-} = \min\left(1, {Q_{ij}^{-}}/{P_{ij}^{-}}\right) \tag{3.27}$$

$$C_{i+\frac{1}{2}j} = \begin{cases} \min\left(R_{i+1j}^{+}, R_{ij}^{-}\right) \; if \, F_{i+\frac{1}{2}j}^{a} \geq 0; \\ \min\left(R_{ij}^{+}, R_{i+1j}^{-}\right) \; otherwise \end{cases} \tag{3.28}$$

The final solution is calculated by applying the corrected antidiffusion coefficient to the diffused low-level solution.

$$\widetilde{F}_{i+\frac{1}{2}j}^{a} = C_{i+\frac{1}{2}j}F_{i+\frac{1}{2}j}^{a} \tag{3.29}$$

$$\rho_{ij}^{f} V_{ij}^{f} = \rho_{ij}^{l} V_{ij}^{f} + \widetilde{F}_{i-\frac{1}{2}j}^{a} - \widetilde{F}_{i+\frac{1}{2}j}^{a} + \widetilde{F}_{ij-\frac{1}{2}}^{a} - \widetilde{F}_{ij+\frac{1}{2}}^{a} \qquad (3.30)$$

A significant amount of time was spent implementing and debugging this algorithm into the existing code as assembled by Mutter. Two cycling schemes were tested using the 2-D FCT algorithm. As a first attempt, the integration cycled through the streamwise and crossplane directions similar to the scheme used by Mutter. Second, the flow was symmetrically integrated, i.e. the cycle progressed through the streamwise and crossplane directions and followed with an integration of the crossplane and streamwise directions, respectively. This process continued until the final time designation was reached. Unfortunately, the solution tended to grow unphysically at the downstream boundary of the computational domain and ultimately "blew-up". After many attempts at resolving this problem, the 2-D algorithm was discarded and the 1-D algorithm was reinstalled as the convective transport integration scheme.

Section 3.3.3 Chemistry Integration

Section 2.5 details the equations describing the chemical kinetics and the application of each of the equations in the flow computation. In this section, the

computational implementation of chemistry and choice of chemistry sub-timestep will be discussed in detail.

The influence of chemistry on species concentrations follows the completion of the convection integration using the timestep splitting technique detailed earlier. Although timestep splitting accuracy depends on small changes in conserved quantities per timestep, large changes in species densities are permitted if the energy density is not affected significantly. Boris and Oran [30] performed a model of a reactive shock and allow changes in energy density of 20% per global timestep.

If we take a closer look at the time scales involved in equations 2.41 and 2.42, we notice that the chemical time scales are much smaller than the convective time scales, and for this reason, the chemical rate equations are described as stiff. For this reason, the chemistry subroutine performs the integration of the rate equations many times with a smaller chemical timestep to resolve smaller chemical transients. A closer look at the chemical time scales and the timestep needed to resolve chemical transients will be looked at later in this section.

Upon completion of the integration of fluid convection, the fluid temperature must be computed in order to evaluate the reaction rates. If heat release is involved, the temperature must be solved from a form of the energy equation because the pressure is

unknown following convection, and therefore, the ideal gas equation of state cannot yield the temperature. The internal energy of the system after convection may be found from the following equation.

$$\varepsilon = E - \frac{1}{2}\rho(\vec{v}\cdot\vec{v}) \qquad (3.31)$$

Assuming that the total internal energy plus the chemical energy remains constant throughout chemistry subcycling, the new temperature may be found by iterating a equation of the following form.

$$\varepsilon + ce_{init} = h\left(T, \{n_j\}\right) - Nk_BT + ce_{cycle} \qquad (3.32)$$

ε is the system internal energy and *ce* denotes the system chemical energy. The subscripts *init* and *cycle* signify the chemical energy at the beginning of a chemical reaction cycling sequence and the chemical energy at each chemical timestep. Using a second order approximation of the internal enthalpy as described in section 2.2, the temperature in equation 3.32 may be solved explicitly. The ideal gas law determines the pressure once the temperature is known.

An instantaneous equilibrium assumption of reactant and product number densities for the first equation proves to be a fair assessment since the relative time scale is much less than the fluid dynamic time scale, and both the forward and backward reaction rates are on the same order of magnitude. The second reaction cannot be assumed to be in equilibrium instantaneously as in the first reaction. At lower temperatures, the rate of production of H_2O greatly exceeds the rate of dissociation of H_2O, in fact, the backward reaction rate was found to change by eight orders of magnitude across the temperatures encompassed in the simulation. Both reactions are described as stiff, in that, the time scales are much smaller than the fluid dynamic time scale.

A number of tests on the chemistry proved to be an efficient and helpful way to determine a reasonable chemistry subcycling timestep. These test will be addressed in further detail in a few paragraphs. The tests singled out a node in the flow field and held the fluid dynamics frozen, similar to the actual timestep splitting technique used in the full simulations. The explicit integrations of the four rate equations (see below) were compared to the integration of the rate equations assuming instantaneous equilibrium in the first reaction.

$$\frac{\partial C_{H_2}}{\partial t} = - k_1^f C_{H_2} C_{O_2} + k_1^b C_{OH}^2 - k_2^f C_{H_2} C_{OH}^2 + k_2^b C_{H_2O}^2 \qquad (3.33)$$

$$\frac{\partial C_{O_2}}{\partial t} = - k_1^f C_{H_2} C_{O_2} + k_1^b C_{OH}^2 \qquad (3.34)$$

$$\frac{\partial C_{OH}}{\partial t} = 2k_1^f C_{H_2} C_{O_2} - 2k_1^b C_{OH}^2 - 2k_2^f C_{H_2} C_{OH}^2 + 2k_2^b C_{H_2O}^2 \qquad (3.35)$$

$$\frac{\partial C_{H_2O}}{\partial t} = 2k_2^f C_{H_2} C_{OH}^2 - 2k_2^b C_{H_2O}^2 \qquad (3.36)$$

Trends in concentrations and temperatures using the equilibrium assumption were similar to the explicit integration, but actual concentrations and temperatures were not completely captured by equilibrium approach in the first reaction. Time scales in each transient differed greatly. Most tests approached equilibrium, except the low temperature test with $X_{H_2O} = 1$ initially, well before the end of a convective timestep. For this reason, integration of a partial convective timestep was completed in order to reduce the chemistry run time needed for the complete 3-D simulation. For the case of $T_{initial} = 1400$ K and $X_{H_2O} = 1$, the backward rate of reaction 2 is minuscule in comparison to the forward and backward rates of reaction 1 and the forward rate of reaction 2, and may be neglected with only minor errors in species number density concentration.

Using the equilibrium assumption for reaction 1, tests were performed to compare concentration and temperature data as the solution proceeded toward equilibrium. A timestep of $5x10^{-18}$ sec. yielded absolute stability for all tests assuming instantaneous equilibrium in the first reaction. Likewise in the explicit integration of all rate equations, $1x10^{-17}$ sec. returned stable values for all tests. As initial mole fractions of hydrogen, oxygen or hydroxyl became large or the initial temperature was large (relative to 1400 K), the integration grew unstable and necessitated such a small timestep. This small timestep proved not to be a problem in the tests using an equilibrium assumption of reaction 1 since the solution approached steady state quickly. This will be discussed in the following paragraphs.

Figures 3.3 and 3.4 show a sample chemistry test using a single node with frozen fluid dynamics. The number densities and temperature as the reaction approaches equilibrium for the equilibrium assumption in the first reaction (Figure 3.4) agrees well with the actual explicit integration results. The transient data in Figure 3.4 seems slightly different than the explicit integration case (Figure 3.3), in that the concentration of hydroxyl molecules shoots up very fast and then relaxes to its equilibrium value. This results from the equilibrium assumption for reaction 1 boosting the concentration of OH molecules to a higher concentration than would physically exist at such early times. Since the energy release and species concentrations at the end of the total chemistry integration are all that need to be determined, this discrepancy is of little interest.

As mentioned previously, a number of tests were performed to determine an acceptable chemical sub-cycling time step. Table 3.1 gives the initial conditions for each test and table 3.2 shows the results at the end of each test. Changes in the number densities of the species were small at the end of most tests for both of the two methods tested, and each test ended well before the convective step (2.8×10^{-7} sec.) finished. This suggests that a partial calculation of the whole convective timestep may be possible to result in reasonable concentrations and temperatures at the end of the chemistry integration. Table 3.2 shows that number densities using the equilibrium assumption for the first reaction produced results that were on the same order of magnitude as the explicit integration results and temperatures that were within a few hundred degrees. As table 3.2 shows, only 100 iterations were used for the method using instantaneous equilibrium for the first reaction and 200,000,000 iterations were used to explicitly integrate all of the rate equations. Of course, the larger number of iterations (200,000,000 as compared to 100) will use a significantly greater amount of computer time. In fact, the tests assuming instantaneous equilibrium for the first reaction required on average approximately 1 second of computer time, and conversely, the explicit integration of each rate equation using 200,000,000 steps used on average 1.4 hours of computer time. These tests assumed that one physical node resided in one computational node, whereas, in the full 3-D simulations more than one physical node will reside in a single computation node. Actually, hundreds of physical nodes may be contained within a single

computational node's memory meaning that the actual time required to simulate combustion in the full simulations may be hundreds of times greater than the 1.4 hours needed for the explicit integration tests.

After weighing the advantages and disadvantages of each method, it was concluded that the instantaneous equilibrium assumption of species number densities for the first reaction yields viable results to evaluate the effects of chemical exothermicity on the flow field and determines concentration trends using an acceptable amount of computer time.

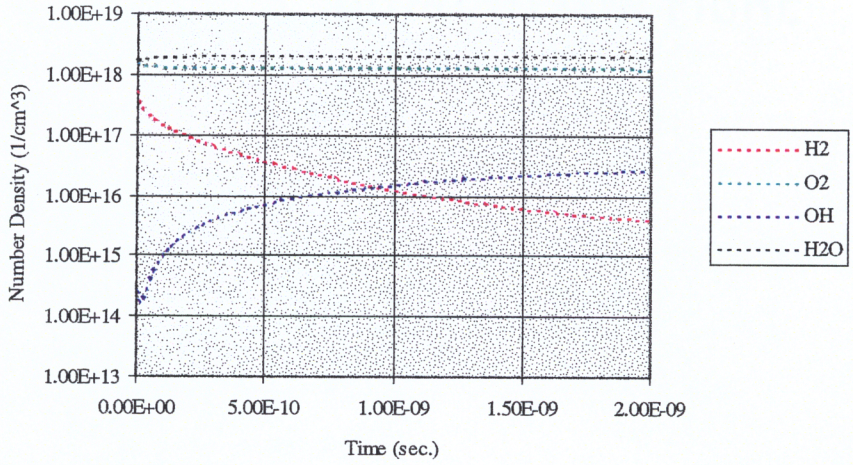

Figure 3.3. Species number density transients explicitly integrating all rate equations: Tinitial = 1400 K; X_{H_2} ***= 0.1,*** X_{O_2} ***= 0.3,*** X_{OH} ***= 0.,*** X_{H_2O} ***= 0.3, and*** X_{N_2} ***= 0.3;*** Δt ***= 1.e-17 sec;*** $n_{iterations}$ ***= 200,000,000.***

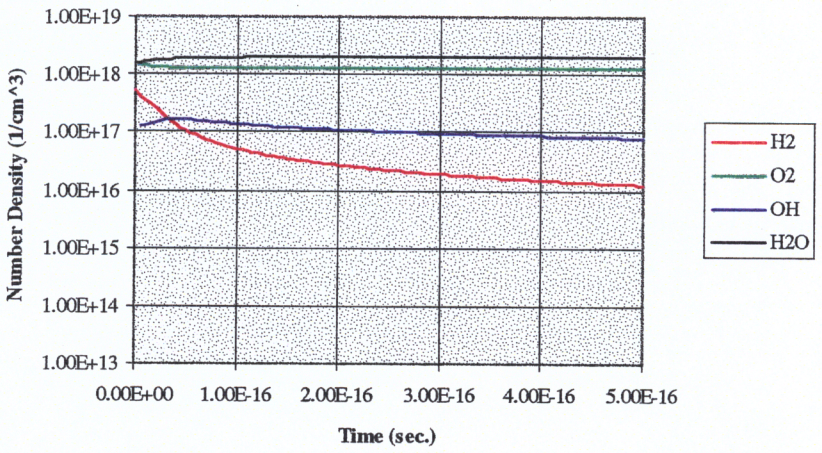

Figure 3.4. Species number density transients assuming instantaneous equilibrium in the first reaction and explicit integration on the second reaction: Tinitial = 1400 K; X_{H_2} ***= 0.1,*** X_{O_2} ***= 0.3,*** X_{OH} ***= 0.,*** X_{H_2O} ***= 0.3, and*** X_{N_2} ***= 0.3;*** Δt ***= 5.e-18 sec;*** $n_{iterations}$ ***= 100.***

Table 3.1. Initial conditions and time step for the test cases

Test #	*Solution Procedure*	*Tinit (K)*	*Pressure (dynes/cm^2)*	X_{H_2}	X_{O_2}	X_{OH}	X_{H_2O}	X_{N_2}	Δt *(sec)*
1	Explicit integration for all rate equations	1400	1.01×10^6	0.1	0.3	0.	0.3	0.3	1×10^{-17}
2	Rxn.1: equilibrium Rxn. 2: explicit integration	1400	1.01×10^6	0.1	0.3	0.	0.3	0.3	5×10^{-18}
3	Explicit integration for all rate equations	1400.	1.01×10^6	0.5	0.5	0.	0.	0.	1×10^{-17}
4	Rxn.1: equilibrium Rxn. 2: explicit integration	1400	1.01×10^6	0.5	0.5	0.	0.	0.	5×10^{-18}
5	Explicit integration for all rate equations	1800.	1.01×10^6	0.2	0.2	0.1	0.2	0.3	1×10^{-17}
6	Rxn.1: equilibrium Rxn. 2: explicit integration	1800.	1.01×10^6	0.2	0.2	0.1	0.2	0.3	5×10^{-18}
7	Explicit integration for all rate equations	1600	1.03×10^6	0.2	0.2	0.	0.2	0.4	1×10^{-17}
8	Rxn.1: equilibrium Rxn. 2: explicit integration	1600	1.03×10^6	0.2	0.2	0.	0.2	0.4	5×10^{-18}
9	Explicit integration for all rate equations	1400	1.01×10^6	0.	0.	0.	1.	0.	1×10^{-17}
10	Rxn.1: equilibrium Rxn. 2: explicit integration	1400	1.01×10^6	0.	0.	0.	1.	0.	5×10^{-18}

Table 3.2. Final concentrations and temperatures for the test cases

Test #	$n_{iterations}$	*cpu time (sec)*	n_{H_2}	n_{O_2}	n_{OH}	n_{H_2O}	*Temp (K)*
1	200,000,000	5036.2	$.405615 \times 10^{16}$	$.130159 \times 10^{19}$	$.276171 \times 10^{17}$	$.207248 \times 10^{19}$	2126
2	100	0.05	$.127079 \times 10^{17}$	$.129268 \times 10^{19}$	$.80527\,4 \times 10^{17}$	$.203737 \times 10^{19}$	2073.2
3	200,000,000	5041.1	$.140434 \times 10^{19}$	$.196850 \times 10^{19}$	$.160544 \times 10^{18}$	$.112831 \times 10^{19}$	3187.7
4	100	0.07	$.271849 \times 10^{18}$	$.143603 \times 10^{19}$	$.254260 \times 10^{17}$	$.232836 \times 10^{19}$	2793.5
5	200,000,000	5016.9	$.487098 \times 10^{18}$	$.731913 \times 10^{18}$	$.788204 \times 10^{17}$	$.130254 \times 10^{19}$	2820
6	100	0.05	$.171813 \times 10^{18}$	$.500023 \times 10^{18}$	$.375807 \times 10^{18}$	$.146933 \times 10^{19}$	3054
7	200,000,000	5071.1	$.316979 \times 10^{18}$	$.614945 \times 10^{18}$	$.394455 \times 10^{17}$	$.152856 \times 10^{19}$	2589
8	100	0.04	$.835394 \times 10^{17}$	$.453942 \times 10^{18}$	$.216578 \times 10^{18}$	$.167344 \times 10^{19}$	2791
9	200,000,000	5058.5	$.100130 \times 10^{15}$	$.214103 \times 10^{14}$	$.114620 \times 10^{15}$	$.522569 \times 10^{19}$	1399.8
10	100	0.06	$.425608 \times 10^{9}$	$.196167 \times 10^{9}$	$.665457 \times 10^{8}$	$.522585 \times 10^{19}$	1400.

Section 3.3.4 Diffusive Transport Integration

Each of the diffusive transport terms, molecular diffusion and thermal conduction, were solved using finite volume techniques. The equations were solved as stated in section 2 using appropriate weighting schemes to evaluate the coefficients of diffusion and thermal conductivity at the cell interface.

Section 4: Simulation Setup

Section 4.1. Setup and Initial Conditions

The results of linear stability analysis evaluated at the inlet plane provided the source of excitation during the calculations. The entire domain was initialized with the basic flow determined by linear stability analysis. The initial temperature and pressure were taken to be 1400 K and 1 x 10^6 dynes/cm^2. Nitrogen and water diluted the oxidizer, O_2, resulting in initial mass fractions of nitrogen, water, and oxygen in the ambient vitiated air mass of 0.544, 0.255, and 0.201, respectively. Nitrogen diluted the fuel, H_2, as well, yielding initial mass fractions of nitrogen and hydrogen in the fuel stream of 0.9 and 0.1. The jet remained subsonic for all times with an initial centerline Mach number of 0.303271 that resulted in an initial centerline velocity of 35,000 cm/sec.

The computational domain consisted of 128 cells in each direction with an extra cell in each direction used to compute interface quantities at the boundaries. The grid was comprised of uniform grid spacing in the streamwise direction and non-uniform spacing in the cross-plane. Within two diameters of the jet centerline in the cross-plane,

the grid size was a constant 0.14 cm. Outside this point, a linear stretching of the grid mesh was imposed allowing a greater physical domain to be used than if the grid stretching had not been used.

Figures 4.1 and 4.2 shows the grid used for examining the calculation results. This grid shown is actually 4 times as coarse in the streamwise direction and twice as course in the cross plane as the computational grid.

Time step choice resulted from testing stability characteristics of convection, and each of the diffusive transport algorithms, molecular diffusion and thermal conduction. Convection proved to be the limiting factor, which necessitated a time step of 2.8×10^{-7} sec. This analysis was based on the Courant condition as shown in equation 4.1,

$$C_r = \frac{(u + a)}{\Delta x}\Delta t \qquad (4.1)$$

where u is the maximum fluid velocity, a is the speed of sound, Δx is the minimum grid spacing and Δt is the time step. For stable flow, the Courant number was chosen to be less than 0.3. The simulations were continued until after a full coherent structure convection time had been reached. Typically, a coherent structure convection speed is equal to one-half of the centerline velocity assuming that the surrounding fluid is

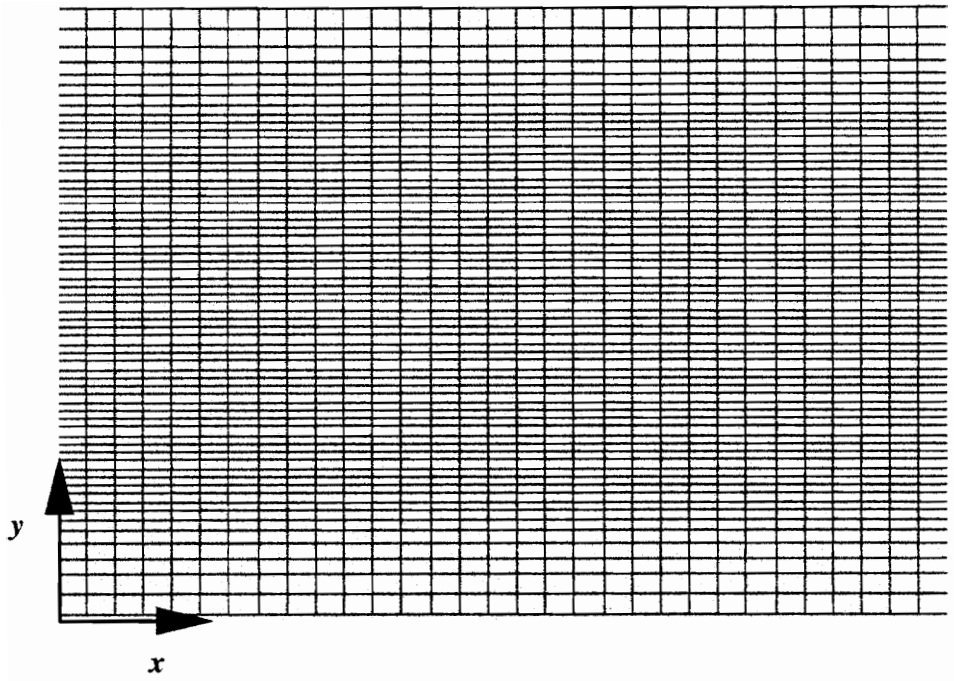

Figure 4.1. Grid used to plot the data: x–y plane (x = streamwise, y = a cross plane direction)

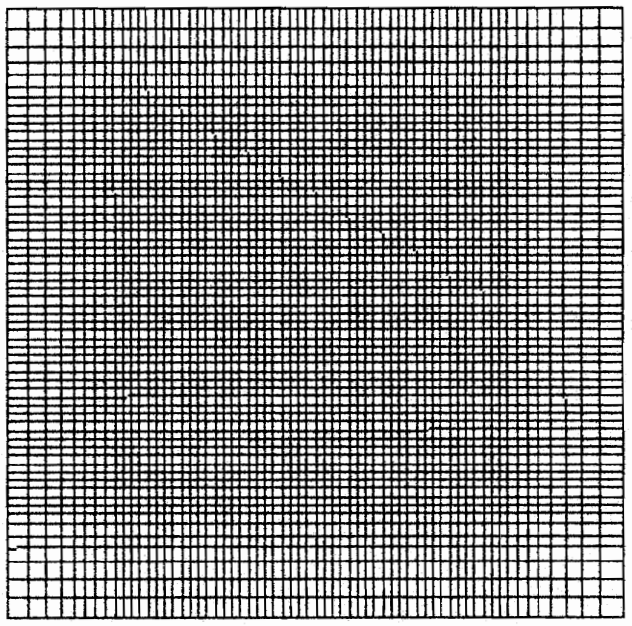

Figure 4.2. Grid used to plot the data: cross plane

quiescent. For both the circular and elliptical jets, coherent structure convection times were approximately 1.68×10^{-3} sec. or 6000 time steps (approximately 6 forcing periods).

Section 4.1. Boundary Conditions

Section 4.1.1 Effects of Boundaries in Spatially Evolving Flows

The solution of a time and spatially dependent flow is no more accurate than the supplied boundary conditions. Boundary conditions are exceptionally difficult to model since free jets generally are described as fluid flows free from any bounding surface, which suggests and infinite domain.

Acoustic disturbances carry information much faster than the convective velocity. These waves propagate in all directions allowing information to proceed out of the computational domain and also enter through the boundaries as well. For this, and many other reasons, boundary condition treatment plays an extremely important role in both reacting and nonreacting flow simulations.

Section 4.2.2 Inlet Boundary

The calculations are excited at the most amplified frequency of the fundamental mode by the results of linear stability analysis (LSA) at the upstream, or inlet, boundary. LSA provides the results of the linearized Euler equations and therefore, supplies the upstream boundary with a realistic representation of the primitive variables. Huang [3] investigated the effects of asymmetric momentum thickness distribution and nozzle geometry on the structure and entrainment capabilities of the jet. The nondimensionalized inlet stability parameters, as used by Mutter [2], and for the present circular jet simulations are given in table 4.1.

Table 4.1. Stability parameters

Stability Parameters	*Circular Jet*	*Elliptical Jet*
ω	1.3	1.2
α_r	1.96	1.70
$-\alpha_i$	0.447	0.433
U_c	35,000 cm/s	35,000 cm/s
R_e	> 2.0 cm	2.0 cm
R_e/θ	7	kept same momentum area as a circular jet
ε	0.02	0.05

All of the quantities given in table 4.1 are nondimensional quantities determined from Huang's [3] linear stability analysis. The growth rate, $-\alpha_i$, and the wave number, α_r, are nondimensionalized by the jet radius, R_e. The temporal frequency, ω, has been nondimensionalized by U_c/R_e, where U_c is the jet centerline velocity. When determining the solution to the linearized Euler equations, as is done in linear stability analyses, one finds an arbitrary scaling factor, ε, preceding the exponential term in the solution (See Huang [1994] for a more in depth analysis), as shown in table 4.1. θ is the shear layer momentum thickness used in the linear stability analysis. The momentum thickness distribution was kept azimuthally constant around the jet periphery.

It should be noted that there was an error in porting the linear stability analysis grid to the simulation, and therefore, the radius of the circular jet is not 2 cm. The radius of the circular jet is approximately 3.5 cm. The results of this simulation are not affected by this, although the simulation could only be extended slightly greater than 4 diameters downstream of the nozzle exit. These results are given in section 5.

The fuel and oxidizer concentrations at the inlet plane follow a hyperbolic tangent profile.

$$Y_F = 0.5\left\{1 + \tanh\left[50\left(\frac{1}{\mu} - \mu\right)\right]\right\} \quad (4.2)$$

$$Y_O = 0.5\left\{1 - \tanh\left[50\left(\frac{1}{\mu} - \mu\right)\right]\right\} \quad (4.3)$$

In the above equations, μ is the radial coordinate in a generalized cylindrical coordinate system. $\mu = 1$ corresponds to the center of the shear layer in an elliptical or circular jet. The mass and oxidizer mass fractions were then converted from the generalized elliptical coordinate system to a uniform Cartesian grid for use as the inlet boundary condition of each of the constituent species. Although the profiles follow a hyperbolic tangent, the factor of 50 preceding the terms in parenthesis essentially makes the profiles resemble top-hat mass fraction profiles, i.e. the gradients of the fuel and oxidizer are huge as the center of the shear layer is approached. Figure 4.3 shows profiles of the fuel and oxidizer mass fractions.

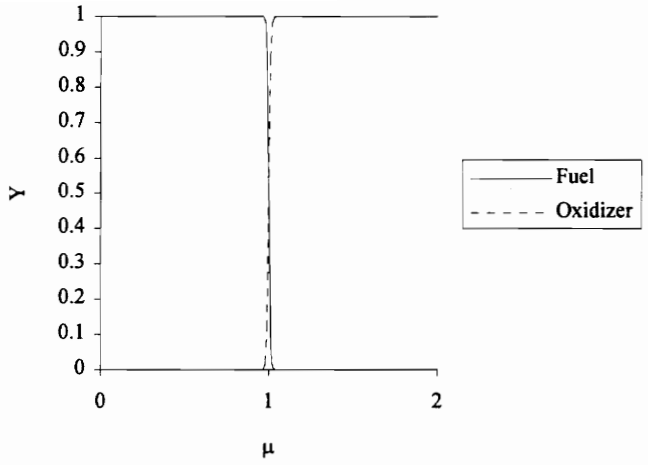

Figure 4.3. Profiles of the fuel and oxidizer mass fractions as a function of the generalized radial coordinate, μ.

Section 4.2.3 Cross-plane Boundary

The simulations assume zero gradient boundary conditions in the cross-plane for all fluid variables realizing that for this assumption to be valid, the jet must be far from the vicinity of the edges of the computation domain in the cross-plane. As Mutter [1994] documented, the zero gradient boundary condition is easily installed in the FCT algorithm. The guard cell values just outside the computational domain are set equal to the cell values just inside the computational domain.

Section 4.2.4 Outlet Boundary

The downstream boundary condition uses an advection scheme suggested by Grinstein [1989]. The conserved fluid quantities are translated out of the computational domain via the local velocity at the downstream location neglecting fluid compression and rotation.

$$\frac{\partial \rho}{\partial t} + u_{loc} \frac{\partial \rho}{\partial x} = 0 \qquad (3.33)$$

The local fluid velocity at the downstream exit, u_{loc}, is determined from an average of the last cell in the computational domain and the guard cell. A zero gradient condition is applied to the pressure.

Section 5: Reacting and Nonreacting Flow Results

Section 5.1. Non-reacting Circular Jet Simulation

Contours of total vorticity with and without superimposed iso-surfaces are shown in figures 5.1 and 5.2 for the nonreacting circular jet, where the shaded region surrounding the jet shows the computational box in the streamwise and cross-plane directions. The jet shear layer remained, for all intensive purposes, parallel until the downstream edge of the computational domain was reached. At this point, the shear layer begins to exhibit a wave-like nature similar to the results found by Mutter [2], although much further downstream. Furthermore, coherent structure formation is suppressed. The structures that develop are quite weak and demonstrate little coherency. Although it is somewhat difficult to make out each structure, the coherent vortices remain planar as convected downstream.

The results of the work of Huang [3] showed that heat release effectively diminished the disturbance growth rate, which may explain the lack of large scale structures found in the circular jet shear layer. Disturbances traveling downstream grow at a slower rate, and therefore, the disturbance level at which roll-up of the shear layer occurs is not encountered until much further downstream. The simulations performed by Mutter had a jet and ambient temperature of 300 K, while the present simulations initialized the simulations with a jet and ambient temperature of 1400 K. This increase of temperature acts like heat release, diminishing the shear layer growth and coherent vortex production. Because of the low level of coherent structure strength, one would expect that vortex merging would not occur until disturbances grew to a higher magnitude significantly farther downstream. For this reason, one would expect little entrainment of ambient fluid into the jet.

Figures 5.3 and 5.4 show contours of hydrogen and oxygen number density, respectively. The lack of coherent vortex production in the computational box culminated in low oxidizer entrainment and therefore, would provide a poor environment for efficient combustion. Because the circular jet would obviously produce less product, create significantly smaller vorticity levels, and entrain less fluid than an elliptical jet, the rest of the circular jet calculations were abandoned and the elliptical jet calculations were begun.

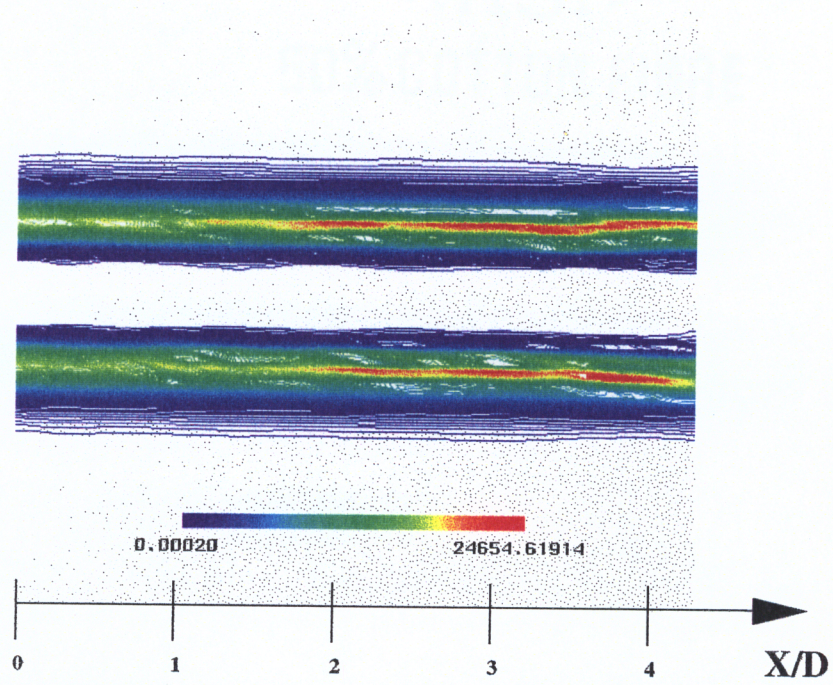

Figure 5.1. Contours of constant total vorticity: time = 9 forcing periods color bar units = 1/sec

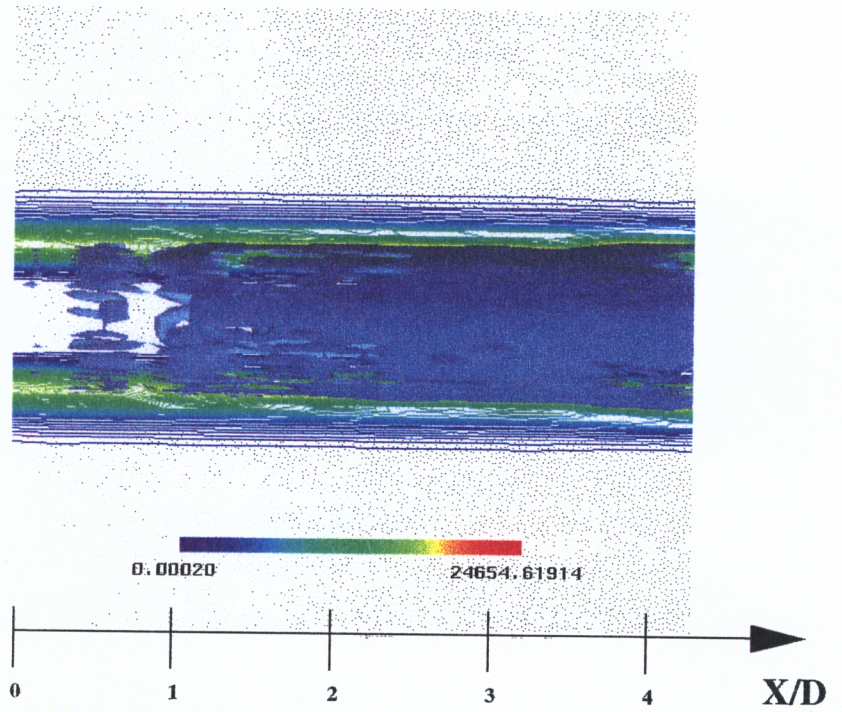

Figure 5.2. Contours of constant total vorticity with superimposed total vorticity isosurface: time = 9 forcing periods; isosurface level = 17753.2 1/sec color bar units = 1/sec

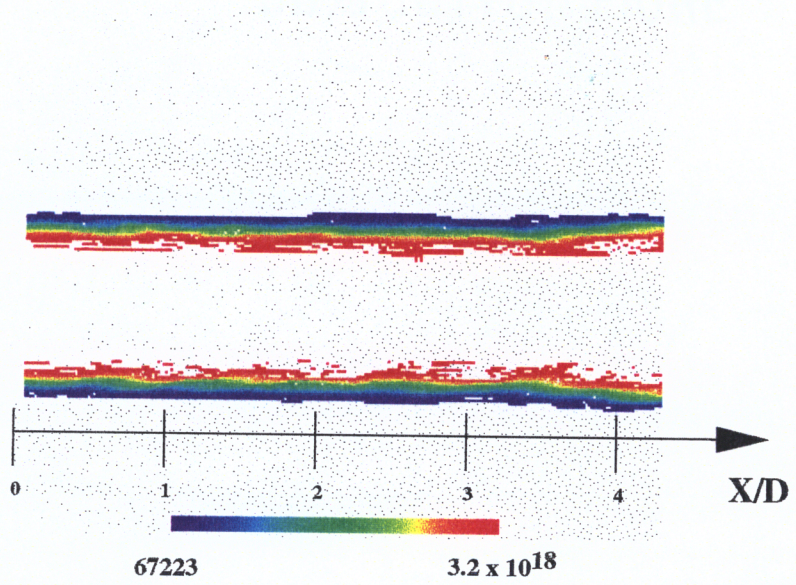

Figure 5.3. Contours of constant hydrogen number density color bar units = 1/cm^3

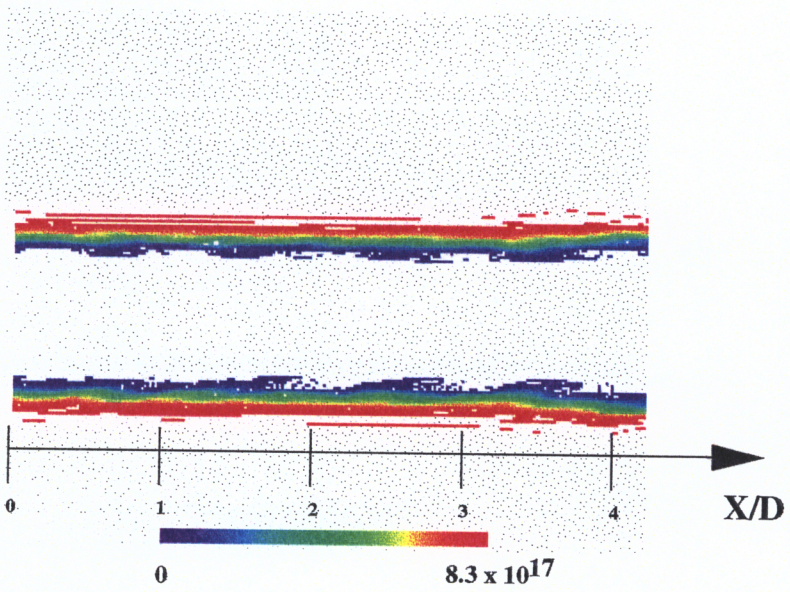

Figure 5.4. Contours of constant oxygen number density color bar units = 1/cm^3

Section 5.2. Elliptical Jet Simulations

Section 5.2.1 Vorticity: Nonreacting Case

Figures 5.5 and 5.6 present the temporal evolution of the nonreacting AR = 2 elliptical jet as illustrated by constant total vorticity contours. In these contours, red is associated with a vorticity level of 40,000 1/sec and above. The values of vorticity lower than 40,000 1/sec are identified by means of the color bar at the bottom of the figure. When viewing these figure it should be noted that the minor axis view refers to a point of view orthogonal to the streamwise and minor axes, i.e. a cut through the plane containing the minor and streamwise axes. Likewise, the major axis view refers to a cut through the major and streamwise axes.

As can be seen in Figure 5.5, the vorticity contours appear similar to the previous circular jet case with small waves in the shear layer until approximately 6 equivalent diameters downstream of the nozzle exit. At this point (at 5 forcing periods), vortex merging occurs on the minor axis forming a larger structure. A similar structure is produced as a result of vortex merging on the major axis as shown in Figure 5.6, although its size and strength is significantly less than its minor axis counterpart. The presence of the new merged vortex structure on the minor axis, shown in figure 5.5 at 6 forcing periods, causes the jet potential core to close upon itself. Pairing of vortices, such as is

shown in Figure 5.5, culminates in a large engulfment of the surrounding ambient fluid into the jet stream providing the first requirement for chemical reaction. Ensuing small-scale mixing delivers the final requirement for combustion.

Mutter [2] found transition from near field behavior to a more turbulent topology to occur approximately 4 1/2 equivalent diameters downstream from the jet exit. At this point, vortex merging occurred and subsequently the jet assumed a more turbulent nature. It is expected that the present simulations would produce such a transition but at a greater length from the nozzle exit due to the increase in temperature of the present simulation. As mentioned previously, temperature increases were found to have a suppressing effect on the growth rate and vortex strength, thereby reducing disturbance magnitudes and suppressing the vortex merging process.

Figure 5.7 shows iso-surfaces of instantaneous constant total vorticity magnitude in the minor axis plane, the major axis plane, and an arbitrary orientation to give the viewer a full sense of the 3-dimensionality of the vortical structures. Clearly, the structures propagate downstream in a out-of-plane fashion with the major axis leading the minor axis as was seen in Mutter's simulations [2] and the experiments of Hussain and Husain [8]. As the structures convect downstream, the minor axis translates faster than the major axis and ultimately catches the major axis approximately 5 1/2 equivalent diameters downstream of the jet exit. Notice that within the last structure shown (closest

to the downstream edge of the computational domain), no coherency is recognizable on the minor axis plane (or the major axis). It is believed that the minor axis structure races by the major axis structure and then breaks up violently, similar to the vortex dynamics explained by Hussain and Husain [8]. The major concentrations of vorticity at the jet exit are shifted off the axes into a region between the crossplane axes.

The explanation for out-of-plane vortex structure growth can be found in the concentration of the total velocity eigenfunction in the minor axis region. Huang [3] showed that for a AR = 2 elliptical jet with non-uniform and uniform momentum thickness distribution that coherent vortices formed earlier on the minor axis than on the major axis. He attributed this out-of-plane formation of the azimuthally oriented vortex structures to the concentration of the total velocity eigenfunction on the minor axis. Disturbances initiated at the jet exit have a higher magnitude on the minor axis than on the major, and therefore, roll-up occurs sooner on the minor axis. This delay in formation on the major axis gave the appearance of the major axis vortex leading the minor axis. This effect is clearly seen in Figure 5.7.

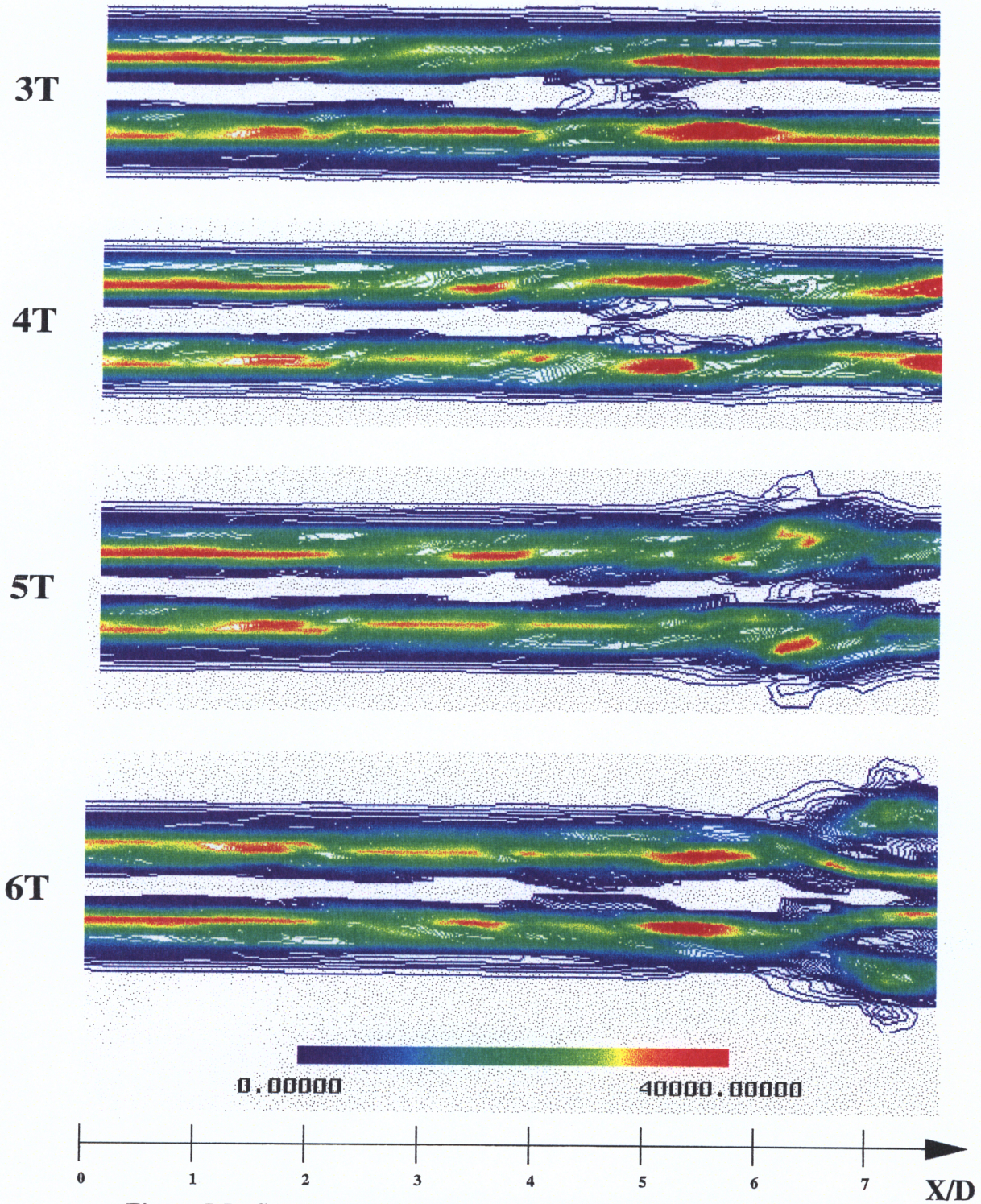

Figure 5.5. Contours of constant vorticity for the nonreacting elliptical jet: minor axis view (color bar units = 1/sec)

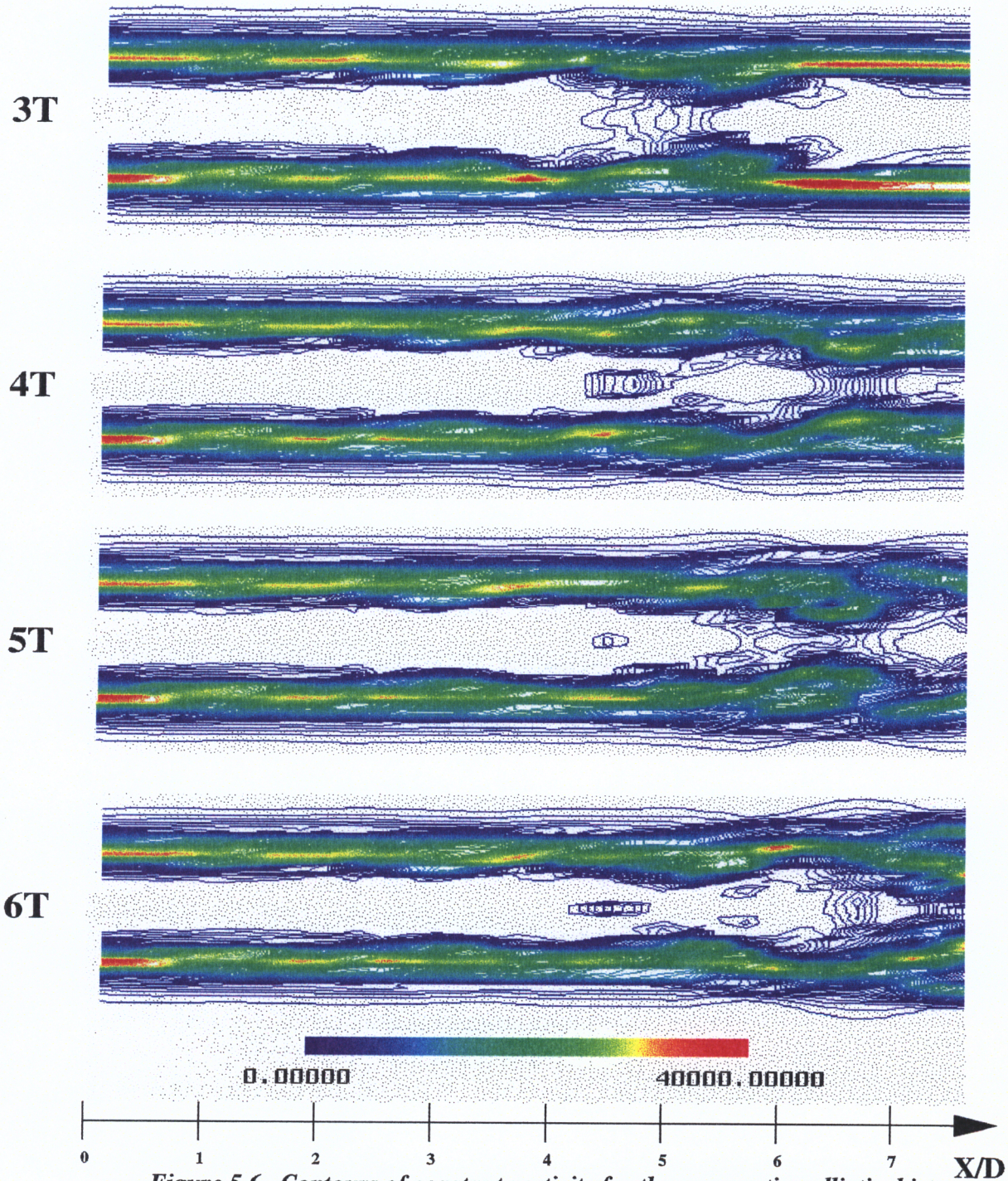

Figure 5.6. Contours of constant vorticity for the nonreacting elliptical jet: major axis view (color bar units = 1/sec)

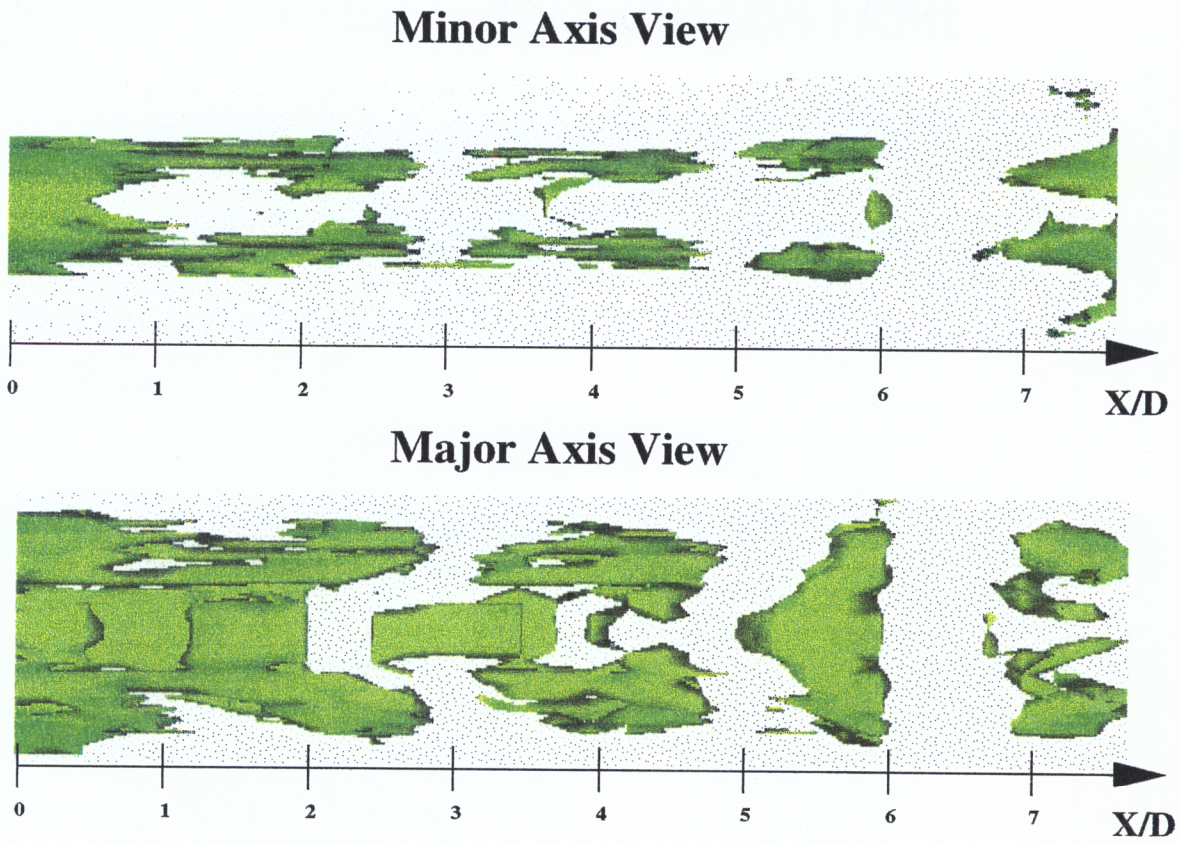

Figure 5.7. Isosurfaces of total vorticity for the nonreacting elliptical jet: isolevel = 31657.8 1/sec

Section 5.2.2 Vorticity: Reacting Case

Figures 5.8 and 5.9 display instantaneous constant total vorticity contours at the indicated times for the reacting flow case. Figures 5.8 and 5.9 may be misleading when comparing them to the previous temporal evolution of the nonreacting flow case. By just looking at the contours themselves, one gets the impression that the total vorticity level is higher in the reacting case than in the nonreacting case. This is not the case. Figure 5.10 shows iso-surfaces of total vorticity for both the reacting and nonreacting jets at an equivalent iso-level. Obviously, the vorticity magnitude has been significantly reduced as a result of chemical reaction, with the largest reduction in the vorticity located off the crossplane axes. In the reacting flow case, vorticity is concentrated on the crossplane axes, and actually produces a higher magnitude of vorticity on each axis than the nonreacting flow. This concentration of the vorticity along the cross plane axes as a result of reaction gives the illusion in the two-dimensional slices that the overall vorticity is higher as a result of reaction.

Notice that vortex merging, as seen in the nonreacting jet, seems to have been suppressed and the potential core appears to persist farther downstream. Since vortex merging provides the primary mechanism for entrainment of surrounding fluid, one would expect reduced oxidizer entrainment, retarded shear layer growth, and less efficient combustion as a result of heat release.

Figure 5.10 displays iso-surfaces of total vorticity for the reacting case. Concurring with McMurtry [20], the vorticity field in the reacting case displayed much less coherency and structure, as well as a reduction in magnitude (the iso-surface level in figure 5.10 is reduced as compared to figure 5.7). Notice, that the iso-surfaces in the reacting case are concentrated on the cross-plane axes thus, giving the illusion in the 2-dimensional plots that the total vorticity in the reacting jet is higher than its nonreacting counterpart.

The coherent vortices appear to convect downstream in a manner not seen in the nonreacting case, and in fact, they appear to convect in a planar fashion similar to circular jets until approximately 6 equivalent diameters downstream from the jet exit. At this point, the jet begins to produce out-of-plane vortex structure typical of most elliptical jets. Because chemical reaction appears to remove the out-of-plane vortex dynamics until further downstream, one would expect that the streamwise component of vorticity to be reduced in the near field region.

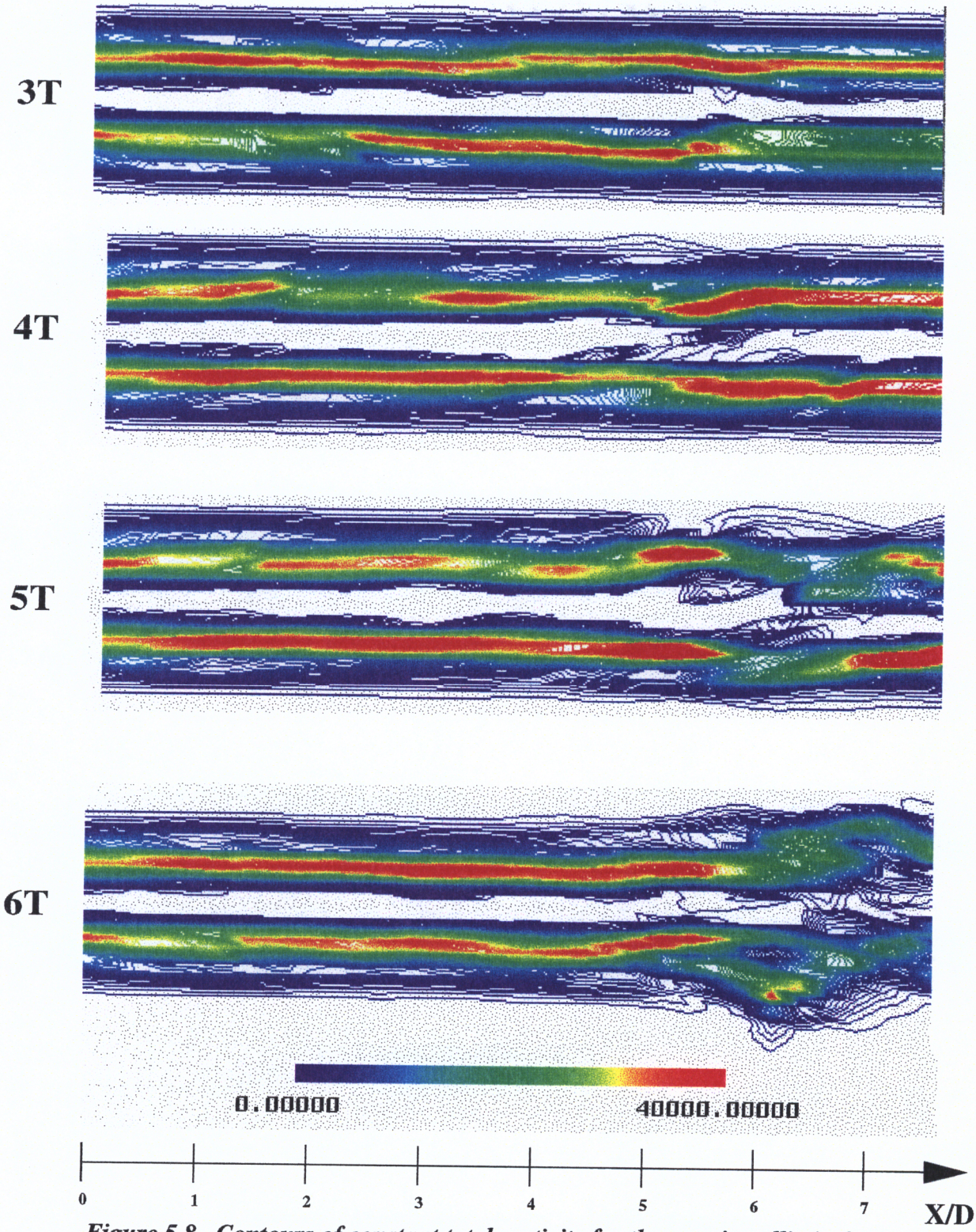

Figure 5.8. Contours of constant total vorticity for the reacting elliptical jet: minor axis view (color bar units = 1/sec)

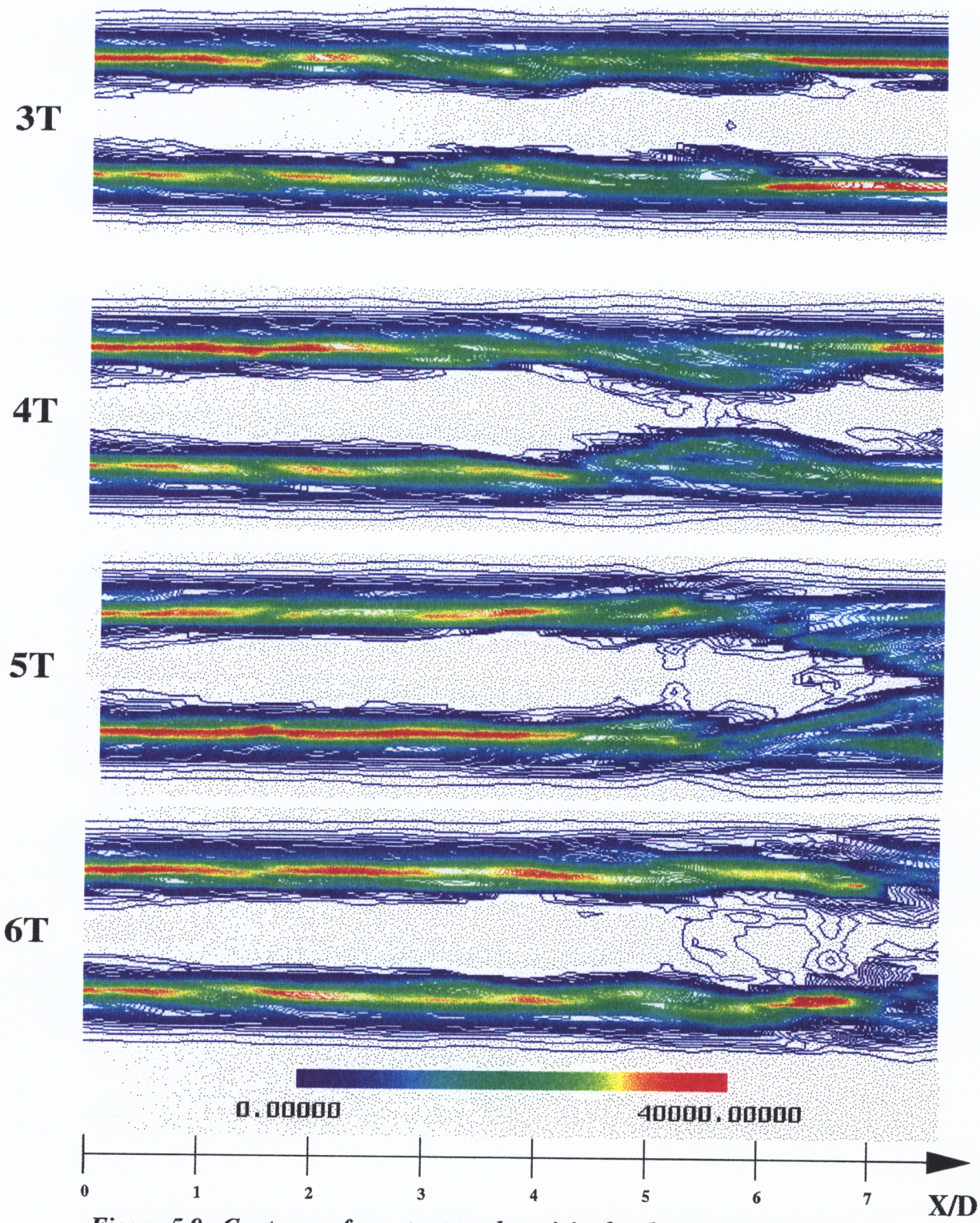

Figure 5.9. Contours of constant total vorticity for the reacting elliptical jet: major axis view (color bar units = 1/sec)

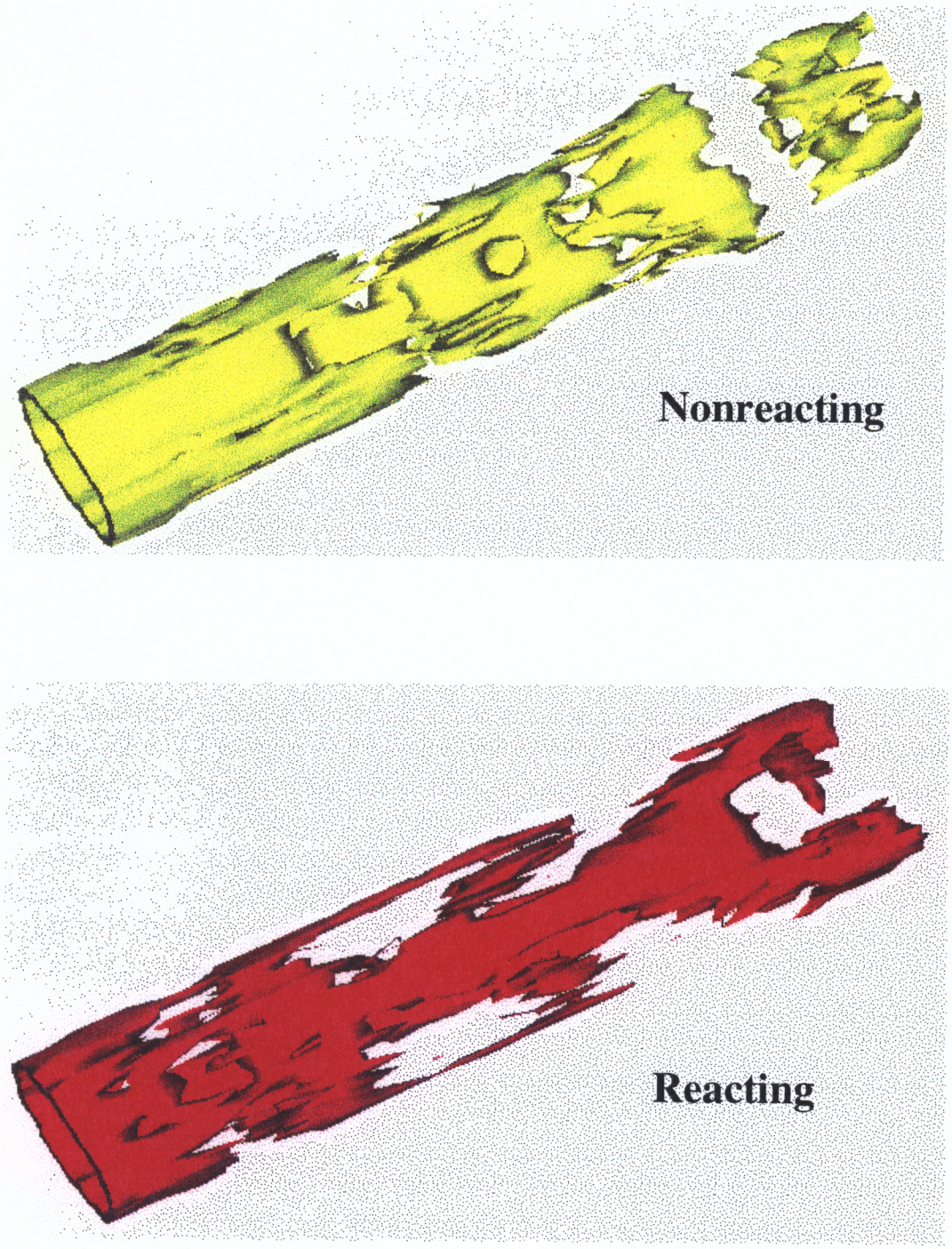

Figure 5.10. Iso–surfaces of both the reacting and nonreacting elliptical jets: iso–level = 29000 1/sec (apx. 1/2 maximum vorticity)

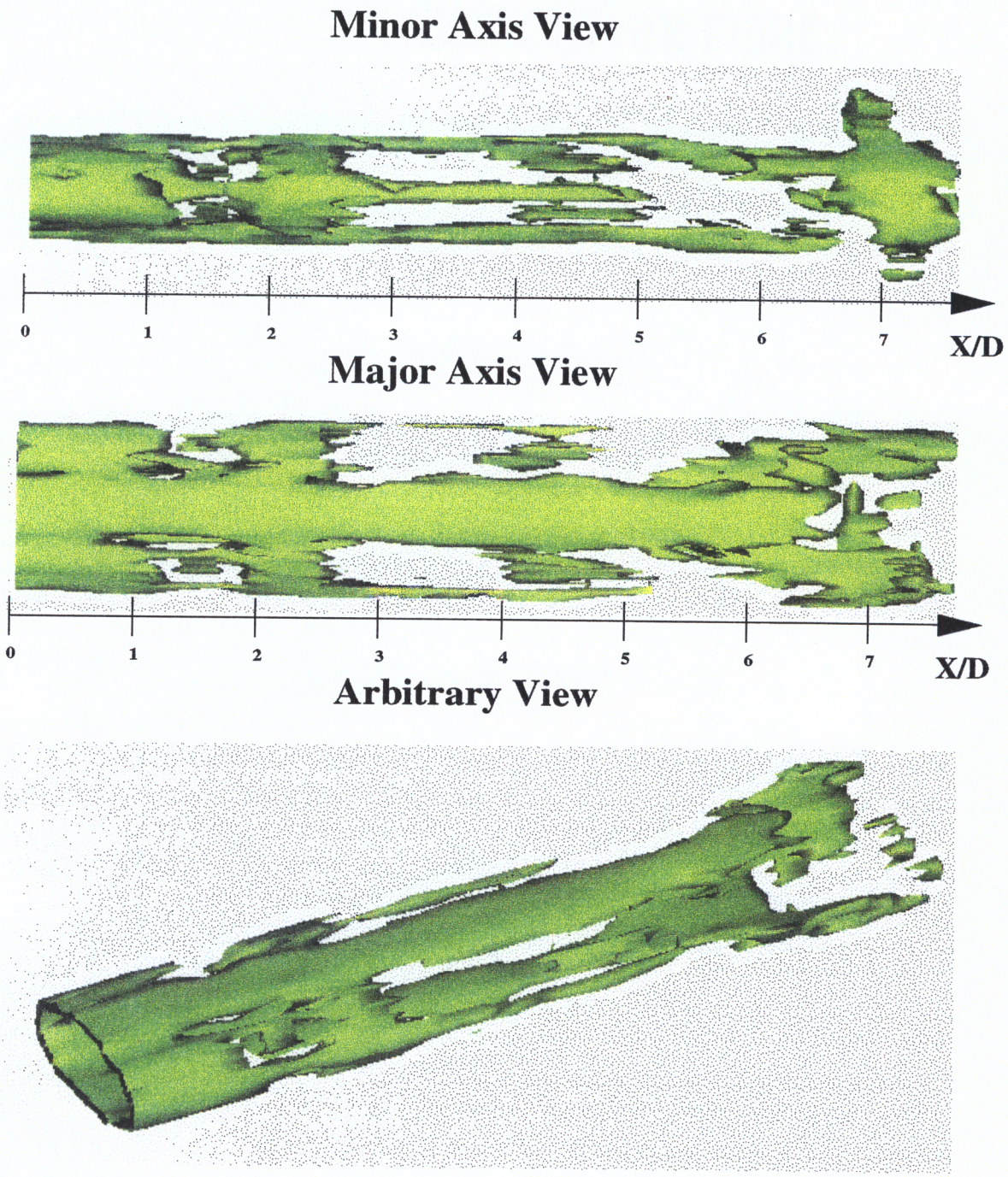

Figure 5.11. Iso–surfaces of total vorticity for the reacting elliptical jet: isolevel = 29397.8 1/sec

Section 5.2.3 Species Concentrations and Temperature

Figure 5.12 and 5.13 display contours of hydrogen and oxygen number densities for both the reacting and nonreacting cases. Figure 5.12 plainly shows the hydrogen being forced into the large vortex structure in the nonreacting case. This type of motion is not seen on the major axis, but rather a spreading of the hydrogen concentration occurs.

Reaction proves to have a significant effect not only on the vorticity field but also on the location of species concentrations. The hydrogen concentration shows a asymmetry about the minor axis not seen in the nonreacting case. Roll-ups of the hydrogen containing shear layer do appear in the minor axis region but not with the size and intensity of the corresponding nonreacting jet, although they certainly appear sooner in the reacting jet than in the nonreacting jet.

Reaction tends to affect a number of topological features of the shear layer as well. As the jet moves downstream, the shear layer appears to change its identity from a varicose topology to a sinuous one. Notice, in figure 5.12 that the nonreacting hydrogen concentration on the minor axis dips in on the top and bottom of the shear layer at a particular axial location and likewise, bulges out on both sides of the shear layer at a particular axial location. This type of jet development is typical of fundamental (varicose) mode forcing. This type of motion can be detected on the major axis as well

but is not as pronounced as on the minor axis. The reacting jet reveals the effects of the fundamental mode forcing in the first half of the computational domain, although it is much harder to detect because the disturbances have not grown sufficiently large to produce this obvious varicose motion. Approximately 3 3/4 equivalent diameters downstream of the upstream boundary, the minor axis region assumes a sinuous shear layer profile, although in the major axis plane the varicose shape seems to have been retained. Reaction apparently has provoked the interaction of multiple modes, and in particular, the interaction of the varicose and sinuous mode shapes.

In addition to topological effects, reaction obviously effects the concentration levels of the constituent species. Figure 5.12 distinctly shows that regions of high hydrogen concentration have been reduced as a result of chemical bonding with oxygen and hydroxyl molecules.

It should be noted that the "blocking off" appearance on the exterior of the hydrogen contours is not due to grid coarseness. Hydrogen gradients in this area are quite minuscule and as a result concentrations are "assumed" to be of equal value. The visualization package can only draw contours in each of the three orthogonal directions, and just by coincidence, the concentrations were approximately equal along the same direction for a number of grid points giving appearance of a coarse grid.

Figure 5.13 presents contours of constant oxygen number density. In the nonreacting case, the oxygen contours follow a trend similar to the hydrogen contours but with different location of maximum and minimum concentrations. Obviously, oxygen concentration is highest in the jet surroundings and lowest in the jet potential core. Examining the effects of reaction on oxygen and hydrogen concentrations shows that oxygen is the limiting factor in the production of hydroxyl radicals. Locations of intermediate hydrogen concentrations, generally associated with green contours in figure 5.12, are evacuated in the oxygen profiles. As a result, the oxygen contours exhibit an increased widening when compared to the hydrogen contours.

Figure 5.14 exhibits contours of constant water number density. Unfortunately, levels of high water density as a result of reaction are not discernible because of the initial concentrations of water in the vitiated air. Future simulations would not use a vitiated air stream, but rather would simply use oxygen diluted with nitrogen to remove this problem. As an additional problem, oxygen was the limiting factor in the reactions, so had the initial oxygen concentrations been higher, additional water would have been produced.

Although water concentrations as a result of reaction are difficult to detect, hydroxyl radical concentrations are not difficult to see. Figure 5.15 displays contours and an iso-surface of hydroxyl number density. High radical concentrations generally define the reaction zone. Figure 5.15 plainly shows that in the near field of the jet, reaction and

therefore, hydroxyl concentrations are contained within the coherent structures. Notice that the iso-surfaces do not display an out-of-plane shape as was seen in the nonreacting jet vorticity field but rather remain planar as they are convected downstream. These iso-surfaces give added evidence to the contention that out-of-plane vortex dynamics is retarded by chemical reaction.

Figure 5.16 shows contours and an iso-surface of jet temperature. High temperature regions are contained solely within the shear layer with highest concentrations found downstream in the larger structures. Higher temperatures would be expected to occur where structures are larger and therefore, oxidizer entrainment is enhanced. Within this location, approximately the downstream half of the domain, the jet maintains an average flame temperature in the vicinity of 2200 K with a high temperature of 3200 K.

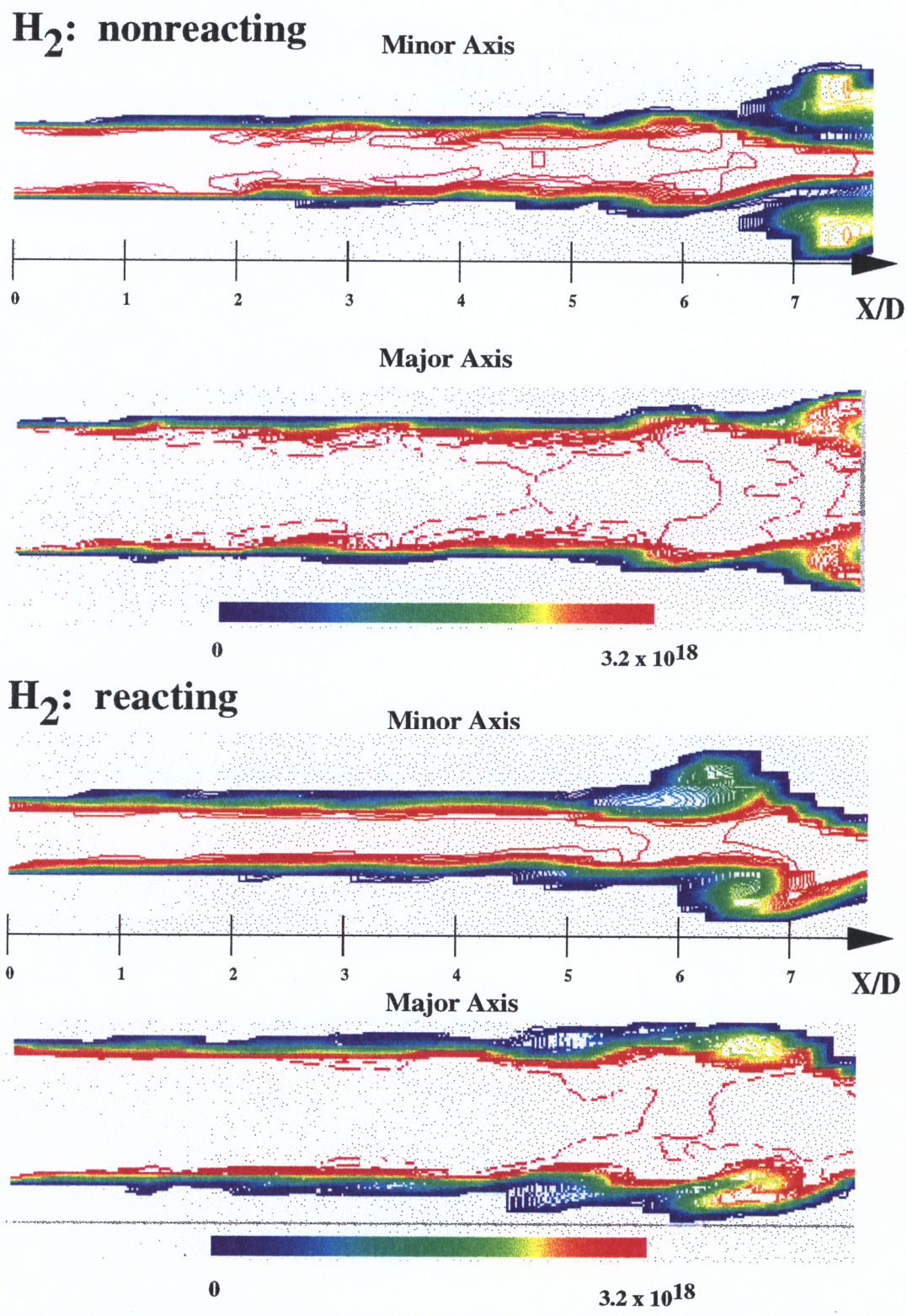

Figure 5.12. H_2 number density contours for the reacting and nonreacting cases: minor and major axis views (color bar units = 1/cm^3)

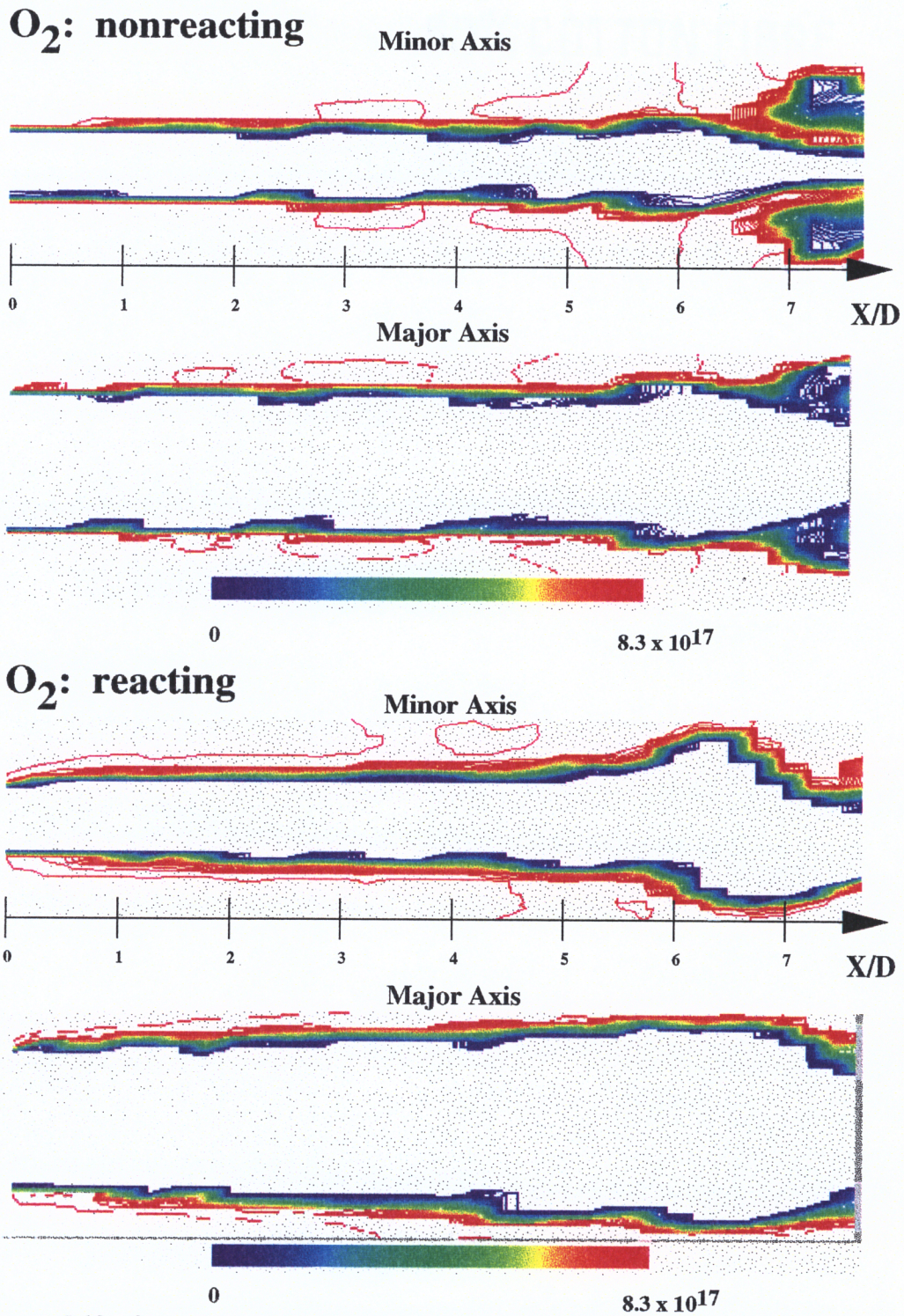

Figure 5.13. O_2 number density contours for the reacting and nonreacting cases: minor and major axis views (color bar units = 1/cm^3)

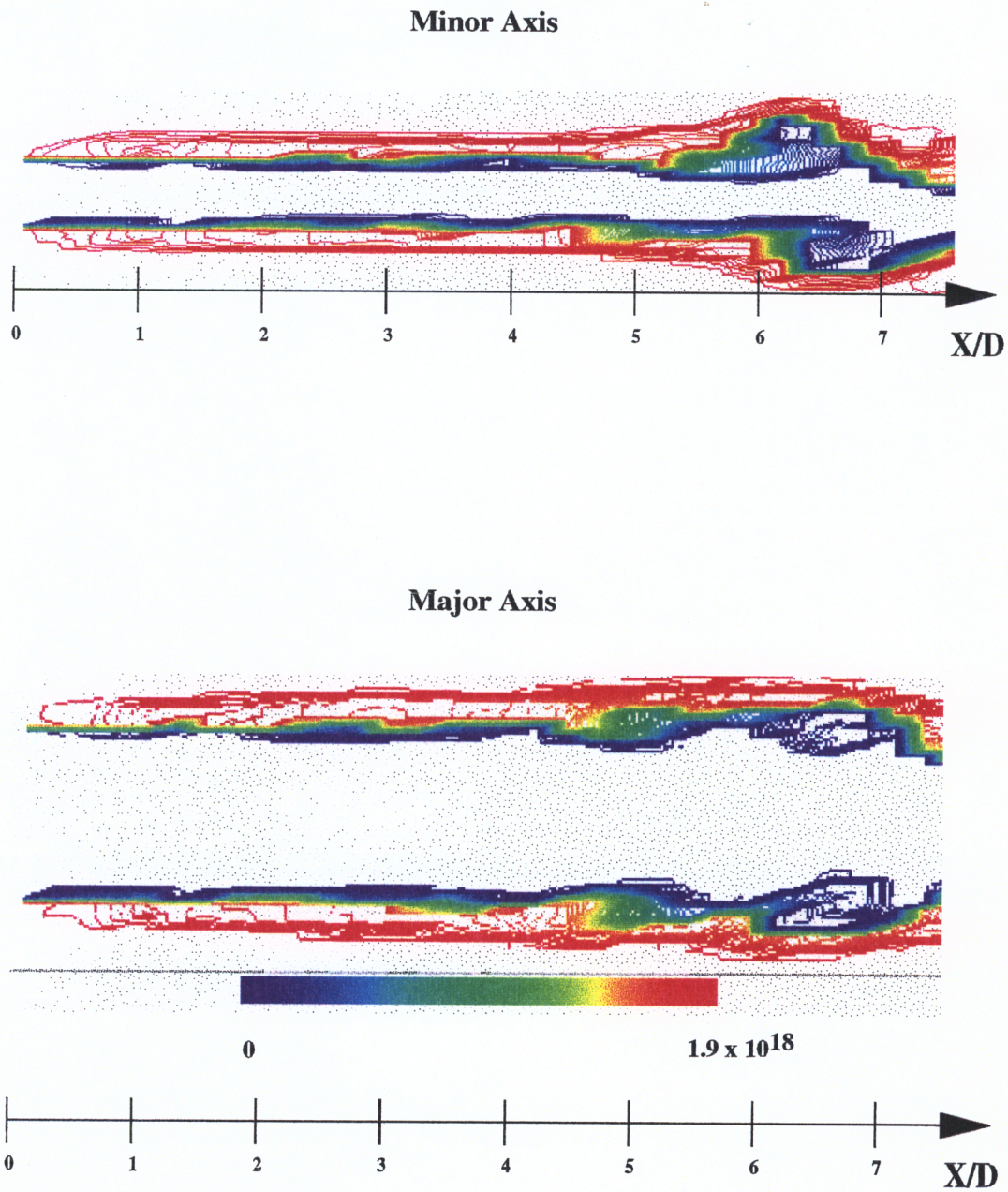

Figure 5.14. Contours of water number density for the reacting elliptical jet: minor and major axis views (color bar units = 1/cm^3)

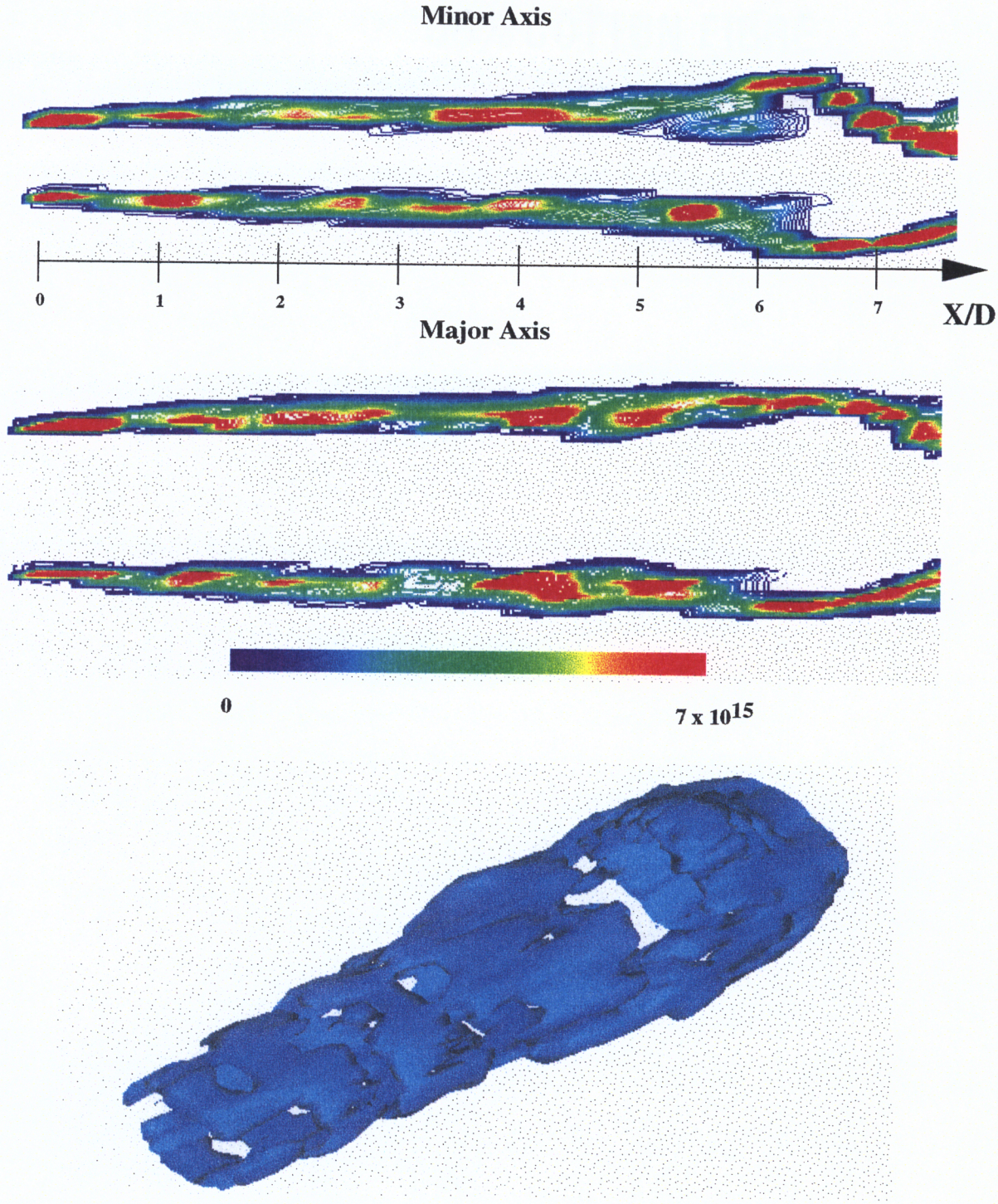

Figure 5.15. Iso–surface and contours of hydroxl number density for the reacting elliptical jet: iso–level = 5.2 x 10^{15} 1/cm^3 (color bar units = 1/cm^3)

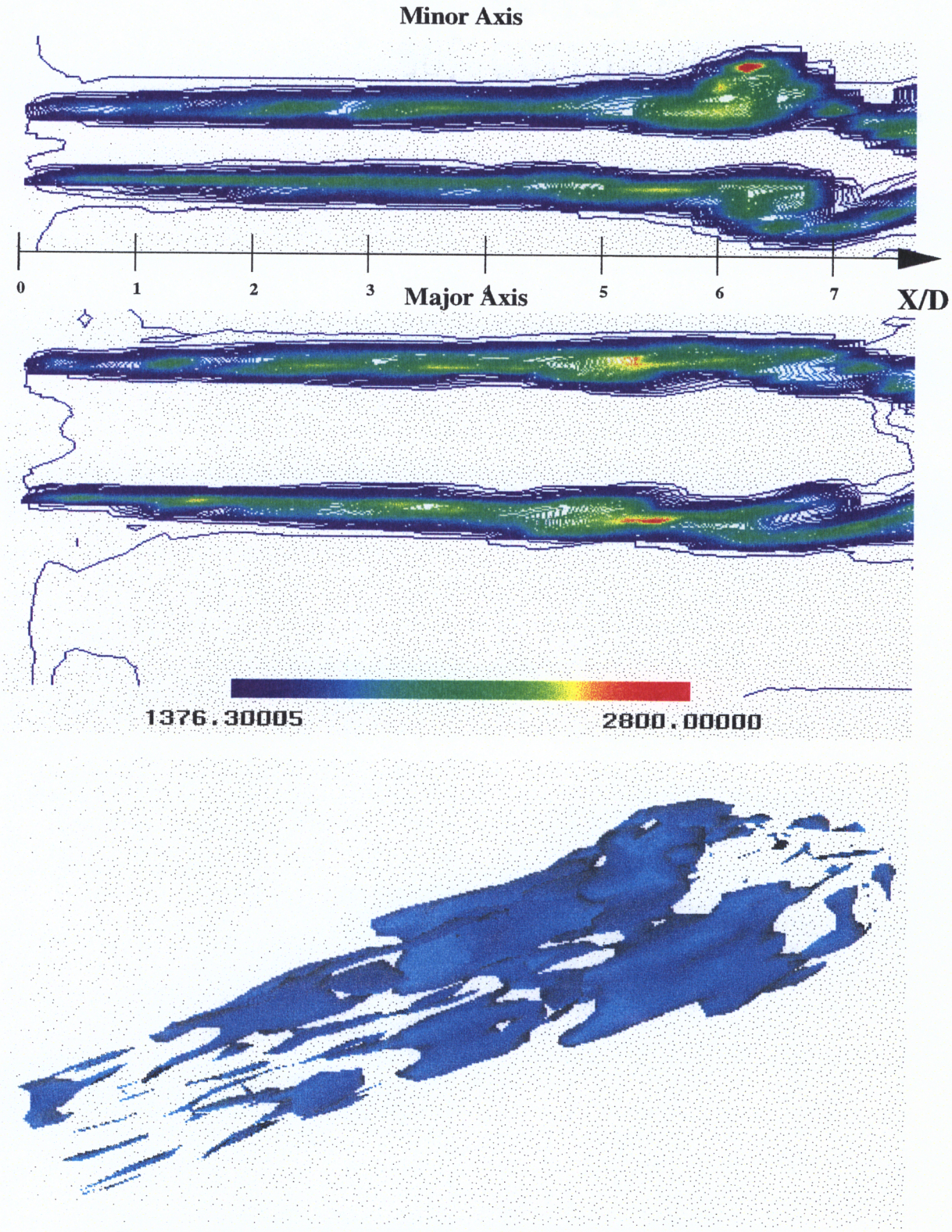

Figure 5.16. Contours and iso–surface of constant temperature: iso–level = 2200 K (color bar units = K)

Section 6: Conclusions

The behavior of elliptical free fuel jets in an oxidizing environment was analyzed in an attempt to determine the effects of chemical reaction on the flow field. In particular, the effects of reaction on large scale vortical structures and their impact on oxidizer entrainment has been addressed.

Three free jet simulations were performed: a nonreacting circular jet, a nonreacting elliptical jet, and a reacting elliptical jet. Each geometry was forced with the results of linear stability analysis at its most amplified frequency. The circular jet showed retarded structure formation when compared to lower temperature circular jet simulations and therefore, lower levels of oxidizer entrainment.

The nonreacting elliptical jet demonstrated out-of-plane vortex dynamics typical of elliptical jets, as seen in many prior research efforts (Hussain and Husain [8] and Mutter [2]). Merging occurred on the minor axis producing a single large scale structure. This structure proved to be the primary mechanism, as seen in this work, for oxidizer

entrainment. The major axis showed lower levels of vortex merging and consequently, less entrainment.

Chemical reaction effectively reduced the level of total vorticity in the jet as well as reducing the overall structure of the vorticity field, as recognized by McMurtry [20]. Coherent structures in the reacting jet showed planar vortex motion more typical of axisymmetric jets. Although the overall vorticity level of the reacting jets was diminished, local concentrations of vorticity were higher in the cross plane axis regions of the reacting jet that the nonreacting jet. Production of hydroxyl radicals was restricted primarily to the regions of high vorticity, and in particular, within the coherent structures. Surfaces of hydroxyl number density also showed a planar ring shape, indicating the structure was, in fact, planar. In addition to reducing the overall vorticity level, reaction caused the minor axis region of the elliptical jet to exhibit a sinuous motion approximately 4 equivalent diameters downstream of the nozzle exit. In addition, the reacting jet retained its potential core further downstream than its nonreacting counterpart.

References

1. Anderson, J. D., *Hypersonic and High Temperature Gas Dynamics*, McGraw-Hill, New York, N.Y., 1989.

2. Mutter, T. B., "Numerical simulations of elliptical jets: a study of jet entrainment," Master's Thesis, Virginia Polytechnic Institute and State University, 1994.

3. Huang, S. L., "Linear stability analysis of non-reacting and reacting elliptical jets," Ph. D. Dissertation, Virginia Polytechnic Institute and State University, 1994.

4. White, F. M., *Viscous Fluid Flow*, McGraw-Hill, New York, N.Y., 1991.

5. Bayly, B. J., Orszag, S. A. and Herbert, T., "Instability mechanisms in the shear flow transition," *Annu. Rev. Fluid Mech.*, vol. 20, 1988, pp. 359 - 391.

6. Ho, C. M. and Huerre, P., "Perturbed shear layers," *Annu. Rev. Fluid Mech.*, vol. 16, 1984, pp. 365 - 424.

7. Ho, C. M. and Huang, L. S., "Subharmonics and vortex merging in mixing layers," *J. Fluid Mech.*, vol. 119, 1982, pp. 443 - 473.

8. Hussain, H. S. and Husain, F., "Elliptic Jets. Part 2. Dynamics of coherent structures: pairing," *J. Fluid Mech.*, vol. 233, 1991, pp. 439-482.

9. Lin, S. J. and Corcos, G. M., "The mixing layer: deterministic models of a turbulent flow. III. The effect of plane strain on the dynamics of streamwise vortices," *J. Fluid Mech.*, vol. 141, 1984, pp. 139 - 178.

10. Monkewitz, P. A., Pfizenmaier, E., "Mixing by 'side jets' in strongly forced and self-excited round jets," *Phys. Fluids A*, vol. 3, no. 5, 1991, pp. 1356 - 1361.

11. Liepmann, D., "Streamwise vorticity and entrainment in the near field of a round jet," *Phys. Fluids A*, vol. 3, no. 5, 1991, pp. 1179 - 1185.

12. Melander, M. V., Hussain, F., "Coupling between a coherent structure and fine-scale turbulence," *Am. Phys. Soc.,* vol. 48, no. 4, 1993, pp. 2669 - 2689.

13. Huang, L. S. and Ho, C. M., "Small scale transition in plane mixing layer," *J. Fluid Mech.*, vol. 210, 1990, pp. 475 - 500.

14. Vuillermoz, P. and Oran, E. S., "Mixing regimes in a spatially confined, two-dimensional, supersonic shear layer," NRL Report # NRL/MR/4404-92-7106, July 1992.

15. Grinstein, F. F. and Guirguis, R. H., "Effective viscosity in the simulation of spatially evolving shear flows with monatomic FCT models," *J. Comp. Phys.*, vol. 101, no. 1, 1992, pp. 165 - 175.

16. Grinstein, F. F., Hussain, F., Oran, E. S., "Vortex-ring dynamics in a transitional subsonic free jet. A numerical study," *Eur. J. Mech., B/Fluids*, 1990, pp. 499 - 525.

17. Grinstein, F. F., Oran, E. S. and Boris, J. P. "Numerical simulations of asymmetric mixing in planar shear flows," *J. Fluid Mech.*, vol. 165, 1986, pp.201-220.

18. Grinstein, F. F., Hussain, F. and Oran, E. S., "A numerical study of mixing control in spatially evolving shear flows," *AIAA* Paper 89-0977, 1989.

19. Ho, Chih-Ming, and Gutmark, E., "Vortex induction and mass entrainment in a small aspect ratio elliptical jet", *J. Fluid Mech.*, vol. 179, 1987, pp. 383-405.

20. McMurtry, P. A., Jou, W. H., Riley, J. J. and Metcalfe, R. W., "Direct numerical simulations of a reacting mixing layer with chemical heat release," *AIAA J.,* vol.24, no. 6., 1986, pp. 962 - 970.

21. Sekar, B. and Mukunda, H. S., "A computational study of direct simulation of high speed mixing layers without and with chemical heat release," Twenty-Third Symposium (International) on Combustion/The Combustion Institute, 1990, pp. 707 - 713.

22. Grinstein, F. F. and Kailasanath, K., "Chemical energy release, spanwise exitation, and dynamics of transistional, reactive, free shear-flows, *AIAA* Paper No. 91-0247, 1991.

23. Grinstein, F. F. and Kailasanath, K., "Chemical energy release and dynamics of transitional, reactive shear flows," *Phys. Fluids A*, vol. 4, n. 10, 1992, pp. 2207 - 2221.

24. Soteriou, M. C. and Ghoniem, A. F., "Dynamics of reacting shear flows; effects of exothermicity and forcing," *AIAA* Paper No. 94-0777, 1994.

25. Vuillermoz, P., Oran, E. S., and Kailasanath, K. "Effect of Damköhler number on a supersonic reactive mixing layer, *AIAA* Paper No. 92-0337, 1992.

26. Russ, S. and Strykowski, P. J., "Turbulent structure and entrainment in heated jets: the effect of initial conditions," *Phys. Fluids A*, vol. 5, no. 12, 1993, pp. 3216 - 3225.

27. Monkewitz, P. A. and Sohn, K., "Absolute instability in hot jets," *AIAA J.*, vol. 26, no. 8, 1988, pp. 911 - 916.

28. Kyle, D. M. and Sreenivasan, K. R., "The instability and breakdown of a round variable-density jet," *J. Fluid Mech.*, vol. 249, 1993, pp. 619 - 664.

29. Oran, E. S. and Boris, J. P., *Numerical Simulation of Reactive Flow*, Elsevier Science Publishing Co., Inc., New York, N.Y., 1987.

30. Boris, J. P. and Oran, E. S., "Detailed modeling of combustion systems," *Prog. Energy Combust. Sci.*, vol.7, 1981, pp. 1 - 72.

31. Chase, M. W., Davies, C. A., Downey, J. R., Frurip, D. J., McDonald, R. A. and Syverud, A. N., *JANAF Thermochemical Tables, Third Edition*, American Chemical Society and the American Institute of Physics, New York, N.Y., 1986.

32. Sonntag, R. E. and VanWylen, G. J., *Introduction to Thermodynamics, Classical and Statistical*, John Wiley & Sons, Inc., New York, N.Y., 1991.

33. Bird, R. B., Stewart, W. E. and Lightfoot, E. N., *Transport Phenomena*, John Wiley & Sons, Inc., New York, N.Y., 1960

34. Mason, E. A. and Marrero, T. R., "Gaseous diffusion coefficients," *J. Phys. Chem.* Reference Data, vol. 1, pp. 3 - 118.

35. Mason, E. A. and Saxena, S. C., "Approximate formula for the thermal conductivity of as mixtures," *Phys. Fluids*, vol. 1, no. 5, 1958, pp 361 - 369.

36. Hirshfelder, J. O., Curtiss, C. F. and Bird, R. B., *Molecular Theory of Gases and Liquids*, John Wiley & Sons, Inc., New York, N.Y., 1954.

37. Dixon-Lewis, G., "Mechanism of inhibition of hydrogen-air by hydrogen bromide and its relevance to the general problem of flame inhibition," *Combust. Flame*, vol 36., 1979, pp. 1 - 14.

38. Kuo, K. K., *Principles of Combustion*, John Wiley & Sons, Inc., New York, N.Y., 1986.

39. Rogers, R. C. and Chinitz, W., "Using a global hydrogen-air combustion model in turbulent reacting flow calculations," *AIAA J.*, vol. 21, no. 4, 1982, pp 586 - 592.

40. Thinking Machines Corporation, Thinking Machines On-Line Documentation: CMview, version 1.3.1, 1995.

41. Boris, J. P. and Book, D. L., "Solution of the continuity equations by the method of the flux corrected transport," In *Methods in Computational Physics*, vol. 16, pp. 85 - 129, Academic Press, New York, N.Y., 1976.

42. DeVore, C. R., "Flux corrected transport algorithms for two-dimensional compressible magnetohydrodynamics," NRL Memorandum #6544, September 1989.

Vita

The author was born on September 26, 1971, to Susan Pyne and Mark Blair in Wilmington, Delaware, and was reared in a suburban community between Wilmington and Newark, Delaware. He attended high school at New Castle Baptist Academy and subsequently enrolled in the University of Delaware in Newark, Delaware, after graduation. The author studied the mechanical engineering curriculum while researching the dynamics of muscular contraction and relaxation with the aim of finding a mathematical model deterministic of muscular force production. After receiving his Bachelor of Science degree in mechanical engineering, the author enrolled in the Virginia Polytechnic Institute and State University. Upon completion of his Master of Science, the author will return to Delaware to embark on a career in computer programming.

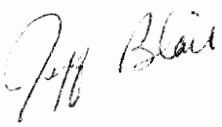

Jeff Blair